Journal of
METAMORPHIC GEOLOGY

J. metamorphic Geol., 2013, **31,** 525–548 doi:10.1111/jmg.12032

An automated method for the calculation of *P–T* paths from garnet zoning, with application to metapelitic schist from the Kootenay Arc, British Columbia, Canada

D. P. MOYNIHAN[1,2] AND D. R. M. PATTISON[1]
[1]*Department of Geoscience, University of Calgary, Calgary, AB, T2N 1N4, Canada (david.moynihan@gov.yk.ca)*
[2]*Yukon Geological Survey, P.O. Box 2703 (K-14), Whitehorse, Yukon, Y1A 2C6, Canada*

ABSTRACT An automated method for the calculation of *P–T* paths based on garnet zoning is presented and used to interpret zoning in metapelitic schist from the southern Canadian Cordillera. The approach adopted to reconstruct the *P–T* path is to match garnet compositions along a radial transect with predictions from thermodynamic forward models, while iteratively modifying the composition to account for fractional crystallization. The method is applied to a representative sample of garnet- and staurolite-bearing schist from an amphibolite facies Barrovian belt in the southern Canadian Omineca belt. Garnet zoning in these schists is concentric and largely continuous from core to rim. Three zones are present, the first two of which coincide with sector-zoned cores of garnet crystals. Similar zoning is developed in rocks that contain or lack staurolite, respectively, suggesting garnet growth was restricted to the initial part of the prograde *P–T* path prior to the development of staurolite. Growth zoning in large garnet crystals has not been significantly modified by diffusion. This interpretation is based on zoning characteristics of garnet crystals and is further supported by results of a forward model incorporating the effects of simultaneous fractional crystallization and intracrystalline diffusion. The *P–T* path calculated for this rock includes an initial, linear stage with a high dP/dT, and a later stage dominated by heating. The approach adopted in this study may have application to other garnet-bearing rocks in which growth zoning is preserved.

Key words: fractionation; garnet zoning; intracrystalline diffusion; *P–T* path; THERIA_G; THERIAK.

INTRODUCTION

Garnet crystals in metamorphic rocks are commonly compositionally zoned, and in favourable circumstances zoning can be used to infer the *P–T* history experienced by a rock during garnet growth. Approaches to gaining information on *P–T* paths from zoned garnet include inclusion thermobarometry (St-Onge, 1987), the Gibbs method (Spear & Selverstone, 1983; Spear *et al.*, 1991; Menard & Spear, 1993) and the use of thermodynamic forward models that predict minerals and compositions as a function of temperature, pressure and bulk composition (Loomis, 1986; Spear, 1988a; Florence & Spear, 1991; Menard & Spear, 1993; Marmo *et al.*, 2002; Tinkham & Ghent, 2005; Zeh, 2006; Gaidies *et al.*, 2008a,b,c).

Compositional zoning in garnet reflects, at a minimum, the interplay of variation in *P–T* conditions, changes in effective bulk composition (EBC- used here as defined in Gaidies *et al.*, 2008a) due to chemical fractionation, and any effects of intracrystalline diffusion during and after garnet growth. *P–T* paths corrected for the effects of chemical fractionation during garnet growth have been calculated by subtracting the composition of the interior of garnet crystals from the whole rock composition (Tinkham & Ghent, 2005; Zuluaga *et al.*, 2005; Zeh, 2006), by assuming Rayleigh fractionation (Evans, 2004), and by matching garnet zoning with predictions from thermodynamic forward models calculated along a defined *P–T* path (e.g. Florence & Spear, 1991; Spear *et al.*, 1991; Gaidies *et al.*, 2008a,b,c). This final approach permits consideration of continuous fractional crystallization (with or without intragranular diffusion) through a rock's *P–T* history. However, because fractionation is path dependent, finding the *P–T* path that best reproduces observed garnet zoning can be difficult.

In this study, the problem of finding the *P–T* path that most closely reproduces garnet zoning in a natural sample is addressed with an automated method that finds a best-fit between observed and modelled garnet compositions, while iteratively accounting for variation in the EBC due to garnet fractionation. The method is applied to garnet + staurolite-bearing metapelitic schist from a Barrovian belt in the southern Canadian Cordillera and used in combination with petrography to reconstruct the *P–T–d* and petrogenetic history of the rock. The schist samples are characterized by well-developed chemical and textural zoning, and contain microstructures that allow integration of *P–T* information with the deformation

history of the area. Further modelling is performed that considers simultaneous fractionation and intracrystalline diffusion, incorporating available geochronological constraints.

GEOLOGICAL SETTING

The Omineca belt of the Canadian Cordillera (Fig. 1a) comprises metasedimentary and metavolcanic rocks of varied age and provenance that were deformed and metamorphosed during Mesozoic to Eocene orogenesis (Evenchick *et al*., 2007). It also includes large volumes of pre-, syn- and post-orogenic plutonic rocks. In the southern Canadian Omineca belt, regional metamorphic grade ranges from greenschist facies to upper amphibolite facies, locally reaching granulite facies (Read *et al*., 1991).

Greenschist to lower amphibolite facies assemblages (M1) and associated structures (D1) developed during initial Cordilleran shortening in the Middle Jurassic and are widely preserved at high structural levels. In parts of the belt, however, these assemblages and structures were overprinted by younger, higher grade assemblages during continued development and eastward propagation of the orogen (Simony & Carr, 2011 and references therein). Episodic metamorphism and deformation continued at some structural levels through the Cretaceous to Eocene, followed by widespread Eocene normal faulting and exhumation. This faulting, an expression of approximate E–W extension, affected a wide area of the southern Omineca belt, and resulted in juxtaposition of rocks with contrasting metamorphic and structural histories (Parrish *et al*., 1988).

The area under consideration in this study lies in the central part of the Kootenay Arc, an eastward-convex curvilinear zone in the southern Omenica belt that is characterized by a distinctive stratigraphy and intense Mesozoic polyphase deformation (Fyles & Hewlett, 1959; Fyles & Eastwood, 1962; Fyles, 1964, 1967; Hoy, 1977; Leclair, 1988). In this area (Fig. 1b), a narrow belt of middle amphibolite facies rocks runs parallel to Kootenay Lake (Archibald *et al*., 1983, 1984; Moynihan, 2012). Metamorphic grade ranges from the chlorite/biotite zones along the flanks of this metamorphic 'high' to the sillimanite + K-feldspar zone in the centre. Along the central part of the lake, the western flank of the amphibolite facies belt is truncated by the west-dipping, Palaeocene–Eocene Gallagher normal fault. South of the bend in Kootenay Lake, another Eocene normal fault – the Purcell Trench fault – marks the eastern boundary of the amphibolite facies belt (Fig. 1b). The study area lies on the NE flank of this metamorphic high, and straddles the boundary between the regional staurolite and kyanite zones.

In the hanging wall of the Gallagher fault, M1 greenschist facies regional metamorphic assemblages were locally overprinted by low-pressure (3.5–4 kbar) contact metamorphic assemblages during intrusion of the Middle Jurassic Nelson batholith (Pattison & Vogl, 2005). Rocks from this region yield Jurassic–Early Cretaceous K-Ar^{40} and $Ar/^{39}Ar$ cooling ages (Archibald *et al*., 1984) and were not affected by later metamorphism or deformation. In contrast, rocks in the footwall, including those that form the subject of this study, underwent peak Barrovian metamorphism (M2) and D2 deformation during the Early Cretaceous, prior to intrusion of an extensive suite of mid-Cretaceous granitic plutons (Leclair *et al*., 1993; Moynihan, 2012). Rocks in this region give Late Cretaceous–early Tertiary K-Ar and $^{40}Ar/^{39}Ar$ biotite and muscovite cooling ages (Archibald *et al*., 1984).

The structure of the central Kootenay Arc is dominated by two generations of gently plunging, approximately N–S-trending folds and associated fabrics (Fyles, 1964, 1967; Hoy, 1980; Leclair, 1988). In the amphibolite facies belt, the dominant fabrics are those associated with the second phase of deformation, which accompanied Early Cretaceous peak metamorphism (Fyles, 1967; Hoy, 1980; Moynihan, 2012). The main schistosity (S2) is axial planar to F2 folds, dips west and is variably developed. Where D2 deformation has been most intense, no evidence of the earlier foliation (S1) is preserved; elsewhere, including the study area, S2 is manifested as a crenulation cleavage of S1.

TECHNIQUES

Mineral compositions were determined using a JEOL JXA–8200 Superprobe at the University of Calgary

Fig. 1. (a) Map showing the location of the study area in the southern part of the Omineca belt of the Canadian Cordillera. The small box shows the outline of Fig. 1b; (b) Metamorphic map of the central Kootenay Arc, showing regional metamorphic isograds, large intrusions and faults. Metamorphic zones define an elongate Barrovian metamorphic high that trends approximately parallel to Kootenay Lake. The samples examined in this study are from the kyanite zone, in the northern part of the metamorphic high. Mineral assemblage and isograd data from Moynihan (2012), Fyles (1964, 1967), Crosby (1968), Hoy (1980), Klepacki (1985), Leclair (1988) and Warren (1997). (c) Map of the study area, showing mineral assemblages in metapelitic rocks and the location of samples discussed in the text. Most of the rocks are garnet-staurolite schists. Kyanite has been reported from one locality in the area but was not encountered during this study. The eye symbol indicates the location and viewing direction of Fig. 1d. (d) Photograph of part of the study area showing the location of samples shown in Fig. 4, taken looking NNW. The samples are from the lower part of the Lardeau Group in a well-defined, continuous stratigraphic sequence on the west limb of the Duncan anticline (Fyles, 1964). The pale coloured rocks in the centre of the image are carbonate units of the Badshot and Mohican formations; stratigraphic younging is towards the right (east).

Laboratory for Electron Microbeam Analysis. Carbon-coated polished sections were analysed at 15 kV using a 20 nA beam and a range of natural and synthetic standards. Garnet, plagioclase and staurolite were analysed using a 5 μm beam diameter. Element-distribution maps of garnet grains were generated

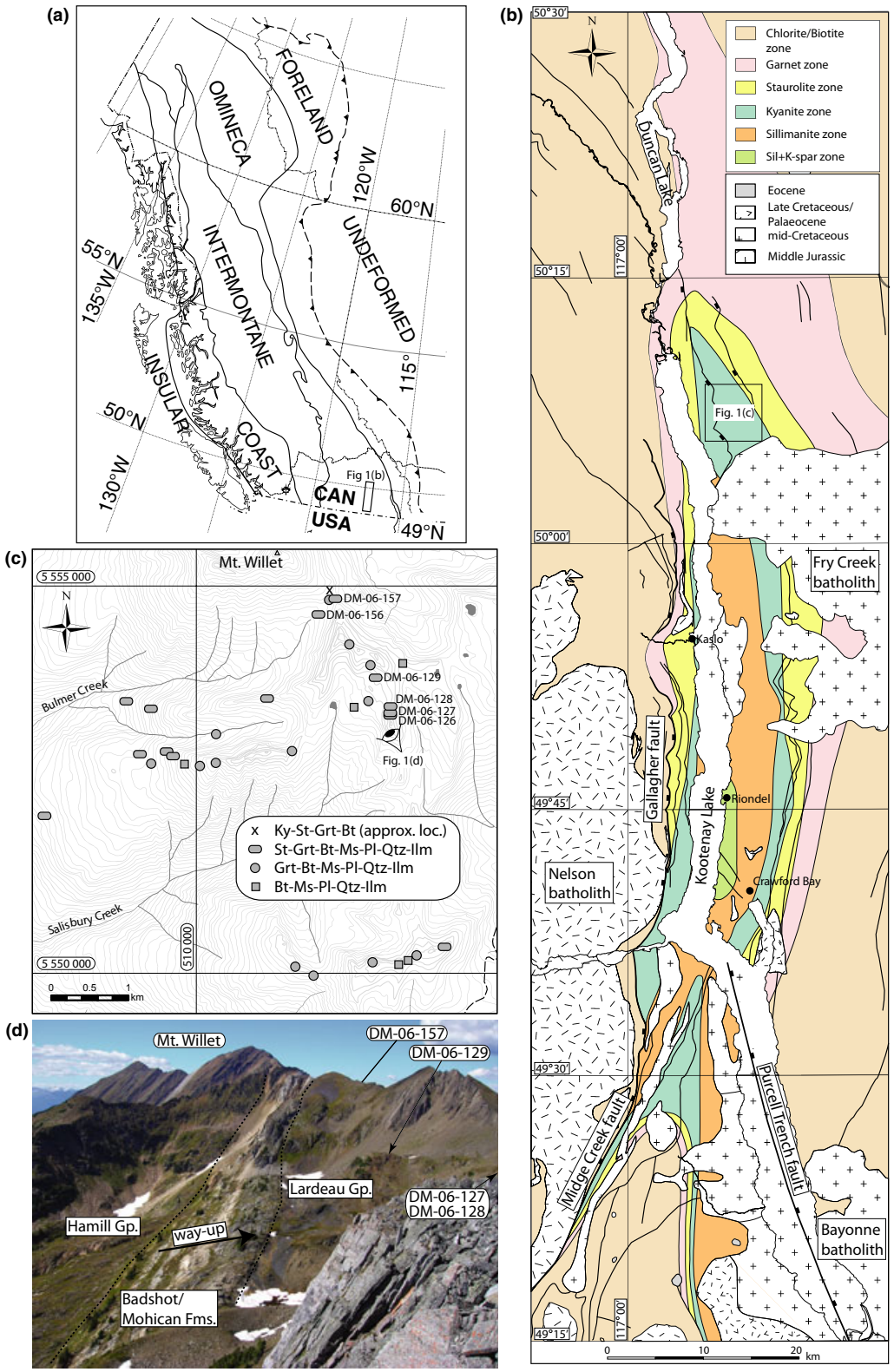

using WDS stage scans for the elements Fe, Mg, Ca, Mn and Y. The mapping was conducted with a focussed beam using step sizes of 2–10 μm, beam currents of 50–200 nA and dwell times of 30–50 ms. Major element chemistry of hand samples was determined by X-ray fluorescence (XRF) using a Philips PW2440 4 kW automated spectrometer system at the McGill University geochemical laboratories, and abundances of S and C established by combustion infrared spectroscopy in the same laboratory.

Thermodynamic modelling was carried out in the 10-component system MnO-Na_2O-CaO-K_2O-FeO-MgO-Al_2O_3-SiO_2-H_2O-TiO_2 (MnNCKFMASHT) using THERIAK/DOMINO (de Capitani & Brown, 1987; de Capitani & Petrakakis, 2010) and THERIA_G (Gaidies *et al.*, 2008a) software in conjunction with version ds5.5 of the Holland & Powell (1998) database. Excess H_2O was assumed, and a melt phase was not considered. For THERIA_G modelling, the garnet diffusion coefficients of Chakraborty & Ganguly (1992) were used, with D^*_{Ca} (tracer diffusion coefficient) set equal to $D^*_{Fe}/2$ (Gaidies *et al.,* 2008a). Activity models used are those outlined in Tinkham & Ghent (2005) with the following exceptions: (i) margarite is not considered as a component in white mica; (ii) the ilmenite–hematite model is that of White *et al.* (2000), with the addition of a pyrophanite component (White *et al.*, 2005), which is assumed to mix ideally; and (iii) a modified version of the White *et al.* (2007) garnet model was used, with $\alpha_{alm} = 1$, $\alpha_{prp} = 1$, $\alpha_{grs} = 3$, $\alpha_{sps} = 1$, $W_{alm,prp} = 2500$ J mol^{-1}, $W_{alm,grs} = 10\,000$ J mol^{-1} and $W_{prp,grs} = 45\,000$ J mol^{-1}. This is the currently preferred model from THERMOCALC version 3.33, extended to include a Mn end-member. The composition used in modelling was derived from the natural composition by eliminating P_2O_5 by projection from apatite. Mineral abbreviations after Kretz (1983) are used throughout the article.

PETROGRAPHY OF THE SAMPLE SUITE

The suite of metapelitic samples was collected from an area of ~25 km^2 close to the northern end of Kootenay Lake (Fig. 1c,d). The rocks are rusty-weathering metapelitic schists with conspicuous mm- to cm-scale garnet porphyroblasts set in a silvery-grey foliated matrix. Many rocks also contain mm-scale staurolite porphyroblasts, while the matrix comprises aligned muscovite and biotite, secondary chlorite, quartz, plagioclase, ilmenite and accessory phases including ubiquitous tourmaline. Rutile, which is partly replaced by ilmenite, was also identified in a single sample.

The assemblage St-Grt-Bt-Ms-Pl-Qtz-Ilm is widely developed in pelitic schists in the area, and a single Ky-St-Grt-Bt assemblage was reported by Reesor (1973). Regionally, this reported assemblage defines the eastern boundary of the kyanite zone; however, kyanite was not found in any samples examined during the course of this study. The reasons for the restricted occurrence of kyanite are unclear, but may reflect some or all of bulk compositional differences, variations in oxygen fugacity or kinetic impediments to the reaction of staurolite to form kyanite (cf. Pattison & Tinkham, 2009; Pattison *et al.*, 2011).

Microstructures

The dominant matrix foliation in the study area (S2) is commonly the sole discernible planar fabric, and relicts of S1 are generally restricted to microlithons within S2 crenulation cleavage. In regions of low D2 strain, however, crenulations of S1 are more open and although axial planes of these crenulations are parallel to S2, the younger foliation is not penetratively developed (Fig. 2a). In some samples, S2 is overprinted by chlorite-rich shear bands.

Garnet porphyroblasts are generally well preserved, though margins are commonly slightly embayed and surrounded by a thin layer of retrograde chlorite. In

Fig. 2. Photomicrographs of rocks from the sample suite. (a) Crenulations of S1 in the matrix of a St-Grt-Bt-Ms schist. The dominant foliation in the area – S2 – is variably developed; in places S1 is fully transposed, elsewhere, S2 forms a crenulation cleavage, with chevron hinges preserved in the matrix. In this location, S1 is crenulated, but an axial planar S2 fabric is not developed. Field of view = 6 mm. DM-06-127. (b) Straight inclusion trails are preserved in a garnet porphyroblast, whereas a crenulation cleavage (S2) is developed in the matrix. S2 wraps around the porphyroblast and open crenulations are preserved in its strain shadow. Field of view = 6 mm. DM-06-126. (c) Inclusion trails define an open fold within a garnet poikiloblast. Field of view = 3 mm. DM-06-156. (d) Crenulations of S1 in the strain shadow of a garnet crystal. S2 forms the matrix foliation and evidence for S1 is only preserved in these strain shadows. The outer part of garnet crystals contain wavy inclusion trails. Collectively, these microstructures indicate synchroneity between garnet growth and D2 deformation. Field of view = 3 mm. DM-06-128. (e) Staurolite crystals aligned parallel to S2, which wraps around a large garnet porphyroblast. Field of view = 6 mm. DM-06-123. (f) Garnet crystal displaying textural zoning. An inclusion-free core with ill-defined sector zoning is surrounded by a zone containing numerous fine inclusions. Outside of this, there is a non-sector-zoned rim with discontinuous alternations of inclusion-free and very inclusion-rich shells. Field of view = 3 mm. DM-06-157G. (g) Graphite accumulations at the end of an inclusion-free column in texturally sector-zoned garnet. See Fig. 3a, area A for a chemical map of the same feature. Field of view = 1.5 mm. DM-06-128. (h) Arcuate zones of graphitic inclusions, resembling cleavage domes (C.D.), on the margin of an inclusion-free garnet core. Field of view = 0.75 mm. A complete photograph and Ca X-ray map of this crystal is included in Fig. 3 (c). Note the contrast between the inclusion-rich areas around the graphite-rich arcs and the inclusion-free rim, and its coincidence with the boundary between garnet zones B and C. DM-06-157G.

some samples, straight inclusion trails across the full width of crystals suggests overgrowth of S1 prior to F2 folding and development of the S2 matrix fabric (Fig. 2b). In others, crenulations are included in garnet crystals (Fig. 2c); in such cases, included crenulations have a longer wavelength and lower amplitude

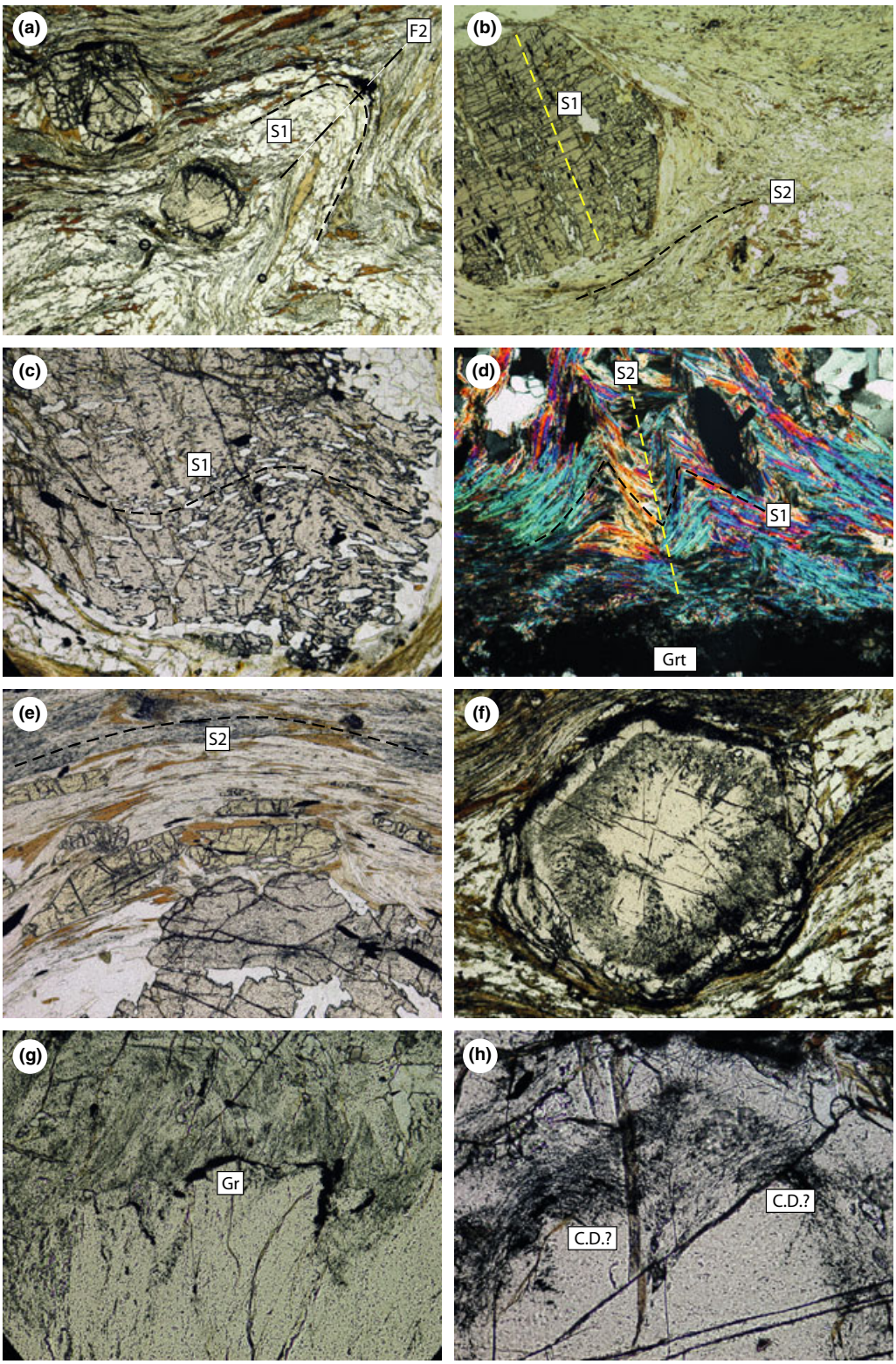

than matrix crenulations. In areas where S2 is well developed, garnet crystals are wrapped by the S2 foliation, and crenulations of S1 are only preserved in the strain shadows of garnet crystals (Fig. 2d). Collectively, these observations suggest that garnet growth preceded and overlapped with F2 folding and the development of S2.

Staurolite porphyroblasts are commonly partly replaced by retrograde chlorite and muscovite. Curved, graphite-rich inclusion trails are common and some larger crystals display sector zoning. Staurolite porphroblasts are generally isolated from garnet, with no replacement relationships evident. Post-staurolite deformation is indicated by quartz-rich strain shadows and locally, their preferred orientation parallel to S2 (Fig. 2e). Dusty, curved inclusion trails are also included in the largest biotite crystals. Biotite crystals, which occur in a wide range of sizes from small matrix grains to porphyroblasts, are extensively replaced by retrograde chlorite. Wrapping of staurolite and biotite porphyroblasts by S2 and the inclusion of curved inclusion trails suggest that staurolite and some larger biotite crystals also grew during D2. Kyanite locally overgrows S2 but intracrystalline strain and a preferential alignment attests to further deformation after its growth. Collectively, the microstructural evidence indicates that D2 deformation and the metamorphism overlapped temporally, with deformation outlasting growth of all porphyroblastic phases.

Textural zoning in garnet

In some samples from the area, the cores of garnet crystals display variably developed textural sector zoning (TSZ) (Fig. 2f,g; Andersen, 1984). In well-developed cases, sector boundaries are marked by lines of inclusions in the core, which branch into broader triangular (in 2-d) inclusion-rich zones in the outer part of the sector-zoned region. Inclusion-free columns extend variable distances into a layer rich in fine inclusions (Fig. 3b), with boundaries that range from sharp to gradational. Whereas in some cases the longest columns extend to the margin of this zone, many do not, resulting in an intermediate, inclusion-rich zone with no discernible sectoral variation (Fig. 2f). The ends of some inclusion-free columns are marked by local accumulations of graphite (Fig. 2g), and in some instances these accumulations outline arcuate shapes (Fig. 2h). These arcuate graphite-rich zones resemble the two-dimensional expression of cleavage domes – a localized domal cleavage that can form at the margin of growing porphyroblasts (Harvey *et al*., 1977; Ferguson *et al*., 1980; Rice & Mitchell, 1991).

In many crystals, the margins of garnet crystals are marked by a complete or partial rim zone that is not sector zoned and generally contains few inclusions. Commonly, this rim is a composite feature (e.g. Fig. 2f), which includes one or more thin, mostly discontinuous, extremely inclusion-rich layers concentrically arranged with inclusion-free shells. These vary within and between garnet crystals, and the clear sectoral and concentric textural zoning described above is not ubiquitous.

GARNET COMPOSITIONAL ZONING

Six samples were selected for chemical analysis, based on their textures and lack of alteration. These samples were collected from a small geographical area within a well-defined, continuous stratigraphic section (Fig. 1d) on the west limb of the Duncan anticline (Fyles, 1964).

The chemical zoning patterns of nine garnet crystals from the six different rock samples were determined by X-ray chemical mapping, with additional reconnaissance work conducted using X-ray line-scans. Four of the samples that were mapped contain the assemblage St-Grt-Bt-Ms-Pl-Qtz-Ilm, whereas two lack staurolite. Significantly, zoning patterns in garnet crystals from five of these samples show broadly similar trends. Although there is some variation in detail between samples, each is characterized by three directly comparable concentric zones (Figs 4 & 5; Table 1).

Fig. 3. Matching photomicrographs and Ca X-ray maps from three garnet crystals displaying textural sector zoning and/or related textures. Warmer colours indicate higher concentrations. Lowest concentrations are indicated by shades of blue, intermediate concentrations by red–pink, and highest concentrations by yellow. (a) and (b) are the largest garnet crystals from DM-06-128, the sample chosen for *P–T* path modelling. They each show textural sector zoning characterized by alternating inclusion-free columns and inclusion-rich segments: in (a), zoning is largely concentric and continuous; however, parts of the zoning record is missing rimward of graphite accumulations (A) and large quartz-filled segments (B). Radial streaks, indicating small difference in Ca concentration parallel to columns, are also visible. A higher magnification photograph of the area marked with a dashed line is shown in Fig. 2g. In (b), inclusion-rich sectors are not as well developed, and there are more complete core-rim transects. The chemical zoning pattern is approximately symmetrical and concentric, whereas the textural zoning is asymmetric; inclusion-poor columns end at different points in the zoning sequence (C lies within high Ca core zone). Inclusion trails outlining crenulations are visible in the outer part of the crystal, including some sector-zoned parts, indicating growth of this part of the crystal after the onset of D2. In (c), arcuate graphitic zones that resemble cleavage domes (C.D.) correspond with embayments with the opposite concavity in the Ca x-ray map (D, E). Part of the zoning scheme is missing rimward of these graphite-rich zones; this is interpreted to reflect a local hiatus in growth due to the graphite accumulation. A higher magnification photograph of the area marked with a dashed line is shown in Fig. 2h. Each of these rocks contains epidote and apatite as inclusions in garnet and as components of the rock matrix.

In zone A (central zone), X_{grs} is flat or increases gradually outwards from a relatively high Ca core (X_{grs} = 0.15–0.25). X_{sps} decreases outwards, from >0.25–0.3 in the core to 0.05–0.1, generally with a steepening of its (negative) slope towards the rim. X_{alm} increases outwards from core values of ~0.5 to

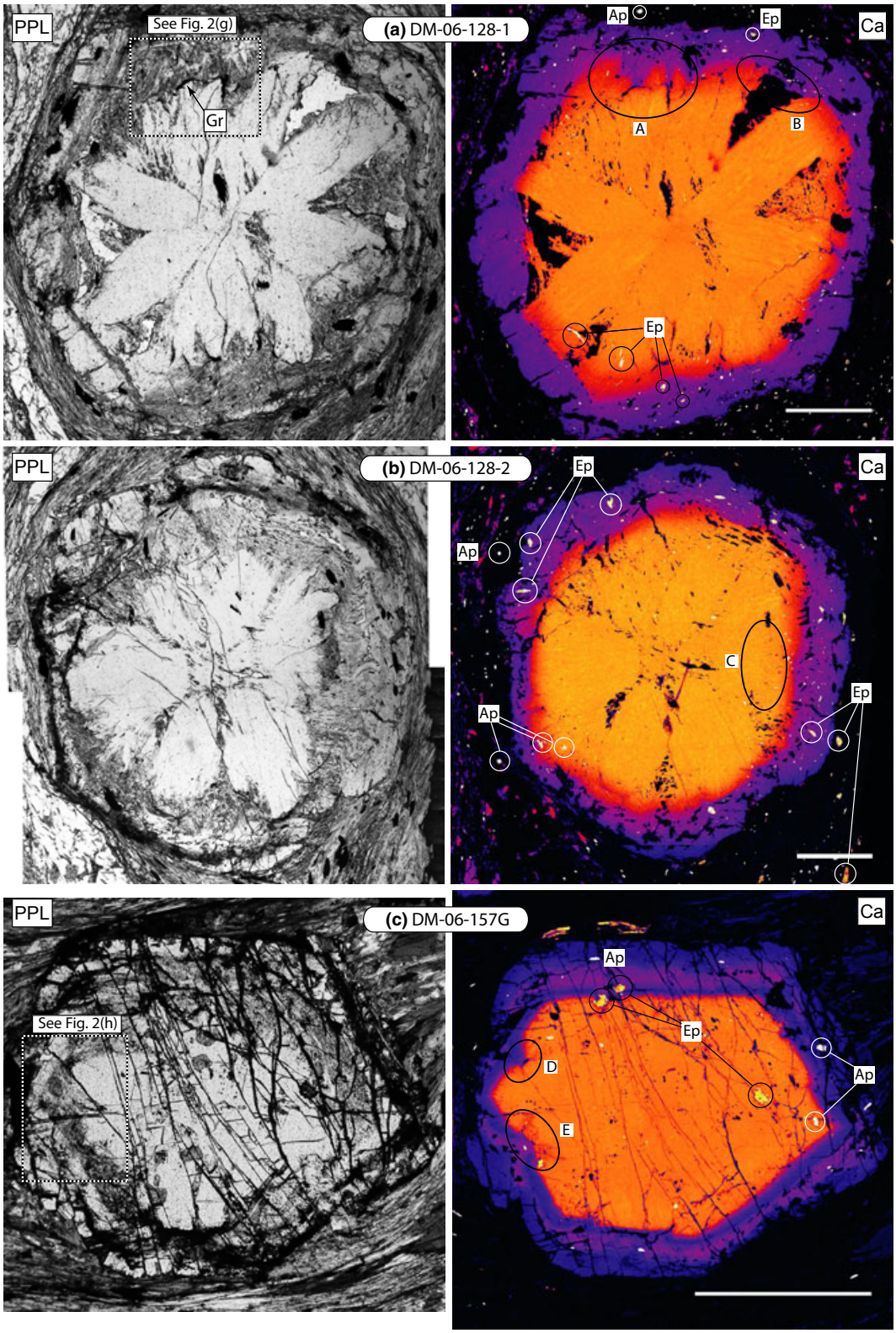

Table 1. Representative mineral analyses from samples discussed in the text.

Sample	DM-06-128	DM-06-128	DM-06-128	DM-06-128	DM-06-128	DM-06-127A	DM-06-127A	DM-06-129B	DM-06-129B	DM-06-157D	DM-06-157D
Mineral	Grt	Grt	Plag	St	St	Grt	Grt	Grt	Grt	Grt	Grt
Position	core	rim	matrix	core	rim	core	rim	core	rim	core	rim
Oxides (%)											
SiO_2	36.41	37.37	61.97	27.91	28.68	36.63	36.25	36.92	36.94	36.95	37.07
TiO_2	0.09	0.00		0.51	0.53	0.08	0.03	0.10	0.00	0.11	0.00
Al_2O_3	20.23	20.61	23.84	55.42	55.19	20.71	20.74	20.56	20.51	20.51	20.76
FeO	22.17	37.30	0.06	11.40	10.29	22.73	38.96	23.39	39.01	21.57	38.48
ZnO				1.86	2.69						
MnO	12.15	0.20		0.06	0.07	13.28	0.28	12.21	0.18	12.18	0.14
MgO	0.54	2.70	0.00	1.10	0.88	0.54	2.59	0.51	2.56	0.35	2.48
CaO	7.51	2.19	4.97	0.01	0.02	5.82	0.82	6.54	0.96	8.44	1.84
Na_2O			8.93								
K_2O			0.07								
BaO			0.01								
H_2O				2.18	2.19						
Total	99.10	100.37	99.85	100.46	100.53	99.78	99.67	100.23	100.17	100.11	100.78
Cations											
Si	2.98	3.01	2.75	3.84	3.93	2.98	2.96	2.99	3.00	2.99	2.99
Ti	0.01	0.00		0.05	0.05	0.00	0.00	0.01	0.00	0.01	0.00
Al	1.95	1.96	1.25	8.99	8.92	1.99	2.00	1.97	1.96	1.96	1.97
Fe	1.52	2.51	0.00	1.31	1.18	1.55	2.66	1.59	2.65	1.46	2.59
Zn				0.19	0.27						
Mn	0.84	0.01		0.01	0.01	0.92	0.02	0.84	0.01	0.84	0.01
Mg	0.07	0.32	0.00	0.23	0.18	0.07	0.32	0.06	0.31	0.04	0.30
Ca	0.66	0.19	0.24	0.00	0.00	0.51	0.07	0.57	0.08	0.73	0.16
Na			0.77								
K			0.00								
Ba			0.00								
H				2.00	2.00						
Sum	8.03	8.01	5.01	16.61	16.55	8.02	8.04	8.02	8.02	8.02	8.02
Norm O	12.00	12.00	8.00	23.00	23.00	12.00	12.00	12.00	12.00	12.00	12.00
Mole fractions											
alm	0.49	0.83				0.51	0.87	0.52	0.87	0.48	0.85
prp	0.02	0.11				0.02	0.10	0.02	0.10	0.01	0.10
grs	0.27	0.00				0.30	0.01	0.27	0.00	0.27	0.00
sps	0.21	0.06				0.17	0.02	0.19	0.03	0.24	0.05
Mg/(Fe + Mg)	0.04	0.11		0.15	0.13	0.04	0.11	0.04	0.10	0.03	0.10
an			0.23								

roughly 0.7, with an increase in its (positive) slope towards the rim. A high Y core is discernible in the centre of zone A in some samples.

In zone B (the intermediate zone), there is a steep drop in X_{grs} to <0.1, coincident with an increase in slope of X_{prp}. The zone is also characterized by a decrease in the (negative) slope of X_{sps} and a continuation or acceleration of the increase in the slope of X_{alm}.

Zone C (rim) is characterized by little radial variation in X_{alm}, a shallow positive slope in X_{prp}, and a shallow negative slope in X_{sps}. A high Y ring coincides with the inner part of this zone. There is some variation in X_{grs} between samples (DM-06-157G contains a small positive Ca annulus), but in each case the overall trend is relatively constant, with a slight rimward decrease.

Three zones are not evident in garnet from the sixth sample analysed; instead, the zoning pattern across the entire radius resembles zone A from the other five samples.

Relationship between garnet compositional zoning and textures

Garnet zoning is mostly concentric and generally continuous; the zoning crosses sector boundaries, and internal compositional boundaries are approximately parallel to the crystal margins. Although there are steep gradients in some elements, the transitions are continuous rather than discontinuous. There are, however, some local anomalies that are related to the internal textures described above. In some instances, a small part of the zoning progression is missing rimward of graphite accumulations (e.g. Fig. 3a,c). The same is also true of some locations rimward of large quartz-filled segments (Fig. 3a). These features suggest that garnet growth was halted temporarily in these sites, while it continued on either side. Around the arcuate features interpreted as possible cleavage domes in Fig. 3c, this has resulted in a pair of chemical embayments with the opposite concavity to that of the graphitic arcs (compare Figs 2h & 3c). While these features are sharpest and most evident in Ca maps, they are discernible in maps of all elements, including Mn.

The texturally sector zoned part of the garnet crystals, and the inclusion-rich layer into which it commonly grades, incorporates chemical zones A and B. Zone B (characterized by a steep drop in Ca) lies close to the tips of inclusion-free columns or adjacent poikiloblastic sectors, but where columns are short, it lies within the inclusion-rich zone. Although there is

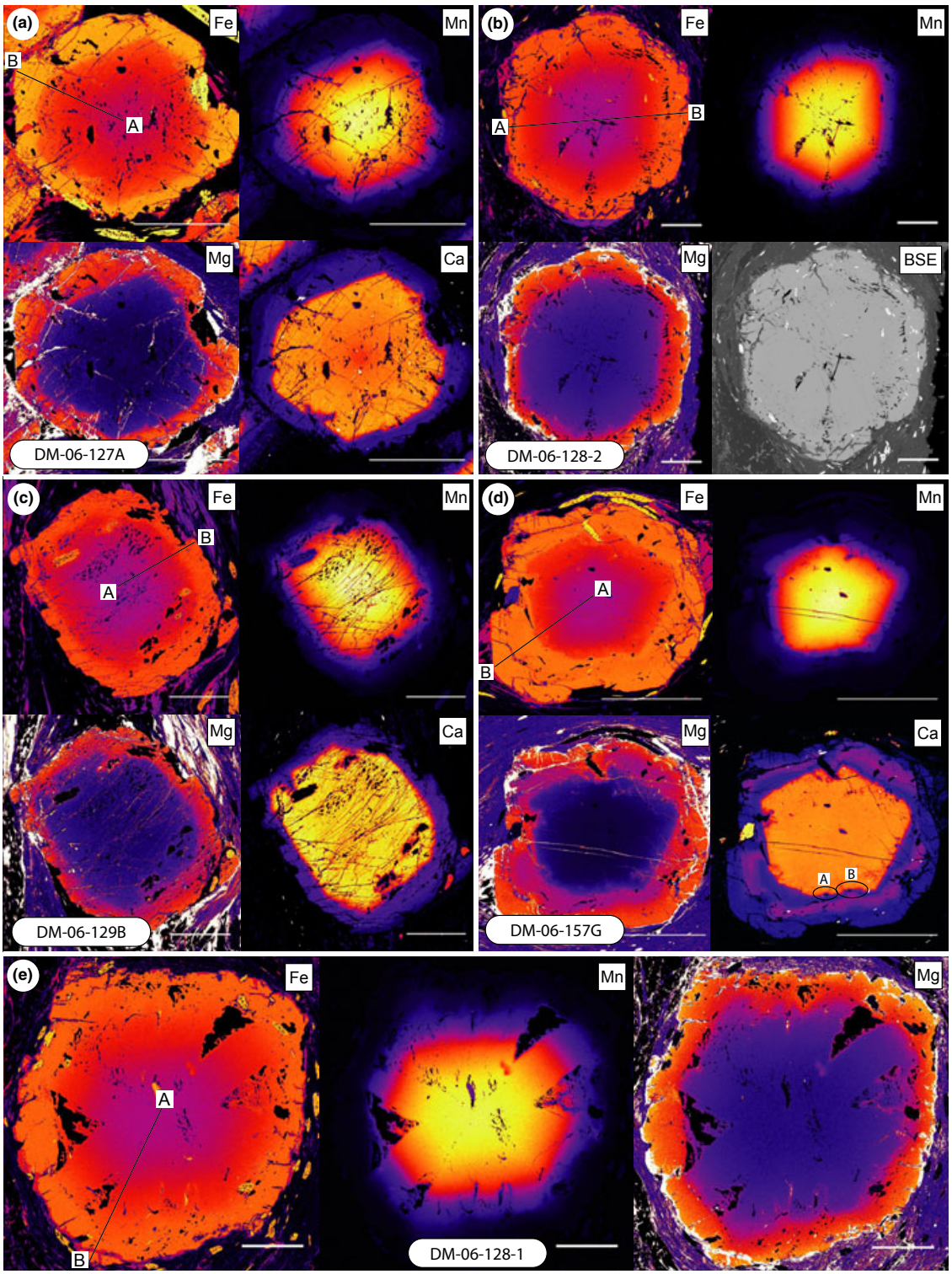

Fig. 4. X-ray maps of garnet crystals from five samples showing relative concentrations of the elements Fe, Mg, Mn and Ca. Warmer colours indicate higher concentrations. Lowest concentrations are indicated by shades of blue, intermediate concentrations by red–pink, and highest concentrations by yellow. The locations of quantitative transects presented in Figs 5 and 6a are also shown. Scale bars are 1 mm. In (b) the Ca map is replaced with a backscatter image as the equivalent Ca map is included in Fig. 3b. The mineral assemblage of the rocks shown in (a), (b), (c) and (e) is St-Grt-Bt-Ms-Pl-Qtz-Ilm. The mineral assemblage in (d) is the same, save for the absence of St from the assemblage. In (d), A, B mark locations where there are steps in the zoning profile around graphite accumulations. X-ray maps in (e) are of the largest garnet crystal from sample DM-06-128, which was used for *P–T* path modelling. A Ca map and photomicrograph of this crystal is shown in Fig. 3a.

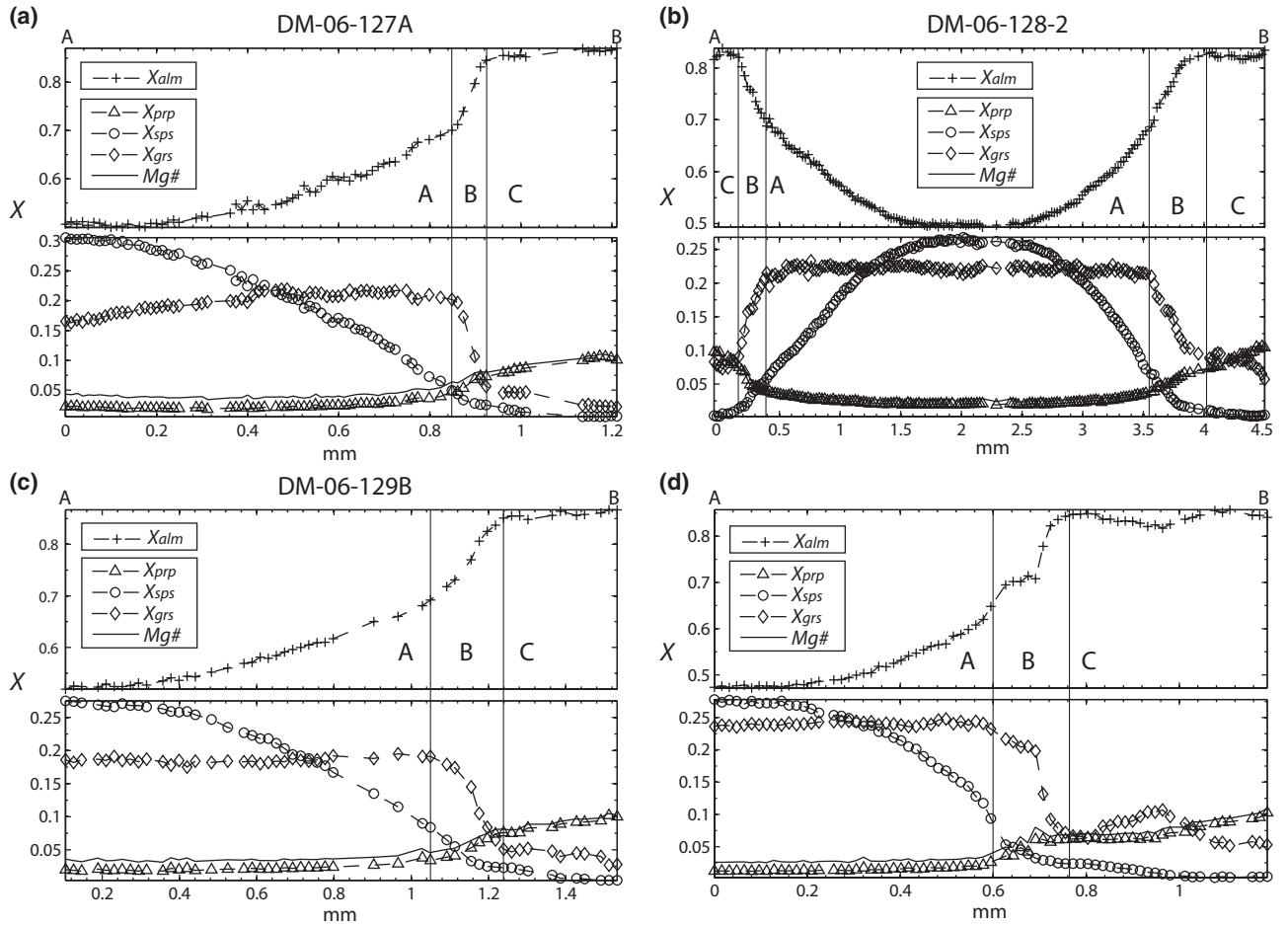

Fig. 5. Garnet composition profiles along the transects shown in Fig. 4a–d. In each of these cases three zones (A, B, C) exhibiting similar zoning patterns can be identified. Mg# = [Mg/(Mg + Fe^{2+})].

not always a clear boundary with the rim, where a boundary is evident, the rim exclusively comprises the low Ca zone.

The only crystal-wide, non-concentric zoning pattern evident in the sample suite is the presence of a second-order, streaky radial fabric in Ca in the central part of some TSZ crystals, parallel to inclusion-free columns (Fig. 3a). These radial streaks reflect lateral differences in Ca content in the order of ~0.01 X_{grs} and are similar to features described by Pattison & Tinkham (2009).

THERMODYNAMIC MODELLING OF DM-06-128

Thermodynamic modelling was carried out with the aim of evaluating the significance of the compositional zoning of garnet in terms of the *P–T* history and metamorphic processes. The sample chosen for detailed modelling – DM-06-128 – is a representative rusty-weathering, silvery grey schist containing porphyroblasts of garnet (0.5–1 cm) and isolated staurolite crystals [~1 mm long; Mg/(Mg + Fe) = 0.13–0.15]. Porphyroblasts are set in a matrix comprising aligned muscovite [(Na/Na + K) = 0.27] and biotite (now partly chloritized), quartz, ilmenite, unzoned plagioclase (X_{an} = 0.23), tourmaline, epidote, apatite and graphite. Garnet contains inclusions of apatite, epidote and graphite. In addition to forming matrix grains, biotite also forms porphyroblasts up to 1 mm long. Approximate modes based on visual inspection are garnet – 7%, quartz – 40%, muscovite – 30%, biotite 11%, plagioclase, 10%, staurolite – 2%.

A single foliation (S2) is evident in the matrix; however, crenulations of S1 are preserved in the strain shadows of large garnet crystals (Fig. 2d). Wavy inclusion trails in the rim of garnet crystals and in the largest biotite crystals indicate overgrowth of F2 crenulations prior to their tightening in the matrix (Fig. 3b), but the timing of folding relative to garnet core growth is unclear. Garnet crystals are variably sector zoned, and have undergone minor

replacement by chlorite along their rims. There are no depletion haloes around garnet crystals.

P–T path modelling was carried out based on a radial profile of the crystal with the largest diameter and highest X_{sps} core composition. This crystal displays well-developed TSZ (Fig. 3a) as well as the tripartite chemical zonation pattern (zones A, B, C) discussed above (Figs 4e & 6a). Radial inclusion trails intersect at a point close to the centre of the crystal, suggesting the analysed section passes through the core of the garnet, allowing measurement of a true radial composition profile. Representative mineral and bulk chemical analyses for this sample are included in Tables 1 and 2 respectively.

In carrying out the modelling, a pure H_2O fluid phase was assumed, whereas the presence of graphite probably resulted in a mixed C-O-H fluid (Connolly & Cesare, 1993) during metamorphism. The discrepancies in the positions of phase boundaries introduced by this simplification are likely to be small, however, at the pressures under consideration in this study (Connolly & Cesare, 1993; Pattison *et al.*, 2002; Pattison, 2006). Although accessory epidote attests to the presence of some Fe^{3+}, Fe_2O_3 was not included as a component in the modelling due to the difficulty of estimating bulk Fe^{3+} at the time of metamorphism and the lack of information about Fe^{3+} contents of other minerals (e.g. chlorite, mica).

Staurolite in this sample contains zinc [Zn/(Zn + Mn + Fe + Mg) = 0.11–0.17], which is also not accounted for in the modelling. It is likely therefore that initial growth of staurolite would occur at a slightly lower temperature than predicted in MnNCKFMASHT. As garnet zoning records growth prior to the growth of staurolite, the absence of Zn from the model chemical system has no significant bearing on the results of the *P–T* path calculations.

Table 2. Bulk composition of DM-06-128 from XRF analysis.

Sample	DM-06-128
	wt%
SiO_2	61.91
TiO_2	0.97
Al_2O_3	17.50
Fe_2O_3	8.89
MnO	0.19
MgO	2.36
CaO	0.87
Na_2O	1.24
K_2O	2.88
P_2O_5	0.14
BaO	1730.70
SO_3	<d/l
	p.p.m.
Ce	77.00
Co	43.22
Cr_2O_3	119.90
Cu	69.85
Ni	38.69
Sc	18.00
V	121.90
Zn	77.00
LOI (%)	3.16
Total (%)	100.34

Predicted phase relations and garnet core isopleth thermobarometry

An equilibrium assemblage diagram (EAD) constructed using the bulk composition of this sample shows that the peak metamorphic assemblage (St-Grt-Bt-Ms-Pl-Qtz-Ilm) is predicted to be stable over a large wedge-shaped *P–T* area between 550 and 650 °C and ~3 and 8 kbar (Fig. 7a). Diagrams constructed for other samples in the suite with the same assemblage yield similarly broad constraints.

Isopleths with values corresponding to those of the garnet core (X_{alm} = 0.49, X_{prp} = 0.02, X_{grs} = 0.22, X_{sps} = 0.27) intersect tightly <10 °C above the equilibrium garnet-in line, at ~500 °C, ~5 kbar (Fig. 6b). The crystal chosen is large relative to others in the rock and the tight intersection of isopleths close to the garnet-in line suggests that only a small amount of the garnet growth history is absent from the analysed sample, assuming equilibrium growth. Whereas isopleth thermobarometry using the bulk composition returns a tight intersection for the core composition, there is no comparable intersection using the rim composition (X_{alm} = 0.82, X_{prp} = 0.10, X_{grs} = 0.08, X_{sps} = 0.00). Grossular and pyrope isopleths intersect, but almandine and spessartine isopleths don't exist within the *P–T* region considered (Fig. 6b).

Forward modelling using a progressively changing bulk composition

A likely explanation for the poor garnet rim isopleth results is that there was a change in the EBC due to fractionation of garnet-forming elements during its growth (e.g. Evans, 2004; Gaidies, 2006). To investigate this possibility, and to seek to reproduce the chemical characteristics of garnet in DM-06-128, forward modelling was carried out using the Gibbs free-energy minimization program THERIAK (de Capitani & Brown, 1987). For a specified bulk composition, THERIAK calculates minerals, compositions, volumes and other thermodynamic parameters along a user-defined *P–T* path, assuming maintenance of thermodynamic equilibrium. These calculations can be made with either a fixed bulk composition, or alternatively in fractionation mode, in which the composition is progressively modified to account for changes in the EBC (de Capitani & Petrakakis, 2010). Here, 100% fractionation was applied to garnet. This represents the end-member case whereby all of the material that is converted to garnet is permanently removed from the modelled composition, which is updated after each *P–T* step.

As chemical fractionation varies depending on the *P–T* path followed, finding a *P–T* path whose modelled chemistry closely matches a natural sample using

this approach involves much trial and error. In this study, the trial and error process was automated by combining THERIAK calculations with a minimization routine in MATLAB. Assumptions inherent in this approach include the following: maintenance of thermodynamic equilibrium during garnet growth, complete fractionation with no garnet resorption, equivalence of the matrix composition and the EBC, and negligible changes in garnet zoning due to intracrystalline volume diffusion during and after garnet growth. This final simplification is discussed further later in the paper.

Calculation of a best-fit *P–T* path using THERIAK in conjunction with MATLAB

A MATLAB script that directs repeated THERIAK calculations was written to calculate a best-fit *P–T* path by minimizing the misfit (χ) between observed and modelled garnet compositions (Fig. 6c). Inputs to the script are the bulk rock composition (X_0), a list of garnet compositions from a radial transect and a starting *P–T* point outside the garnet stability field (P_0,T_0).

For the purpose of these calculations, the misfit (χ) is defined as:

$$\chi=\sqrt{\left(\frac{\chi alm_{\mathrm{obs}}-\chi alm_{\mathrm{mod}}}{\chi alm_{\mathrm{obs}}}\right)^2+\left(\frac{\chi gr_{\mathrm{obs}}-\chi gr_{\mathrm{mod}}}{\chi gr_{\mathrm{obs}}}\right)^2+\left(\frac{\chi sps_{\mathrm{obs}}-\chi sps_{\mathrm{mod}}}{\chi sps_{\mathrm{obs}}}\right)^2}$$

where the subscripts $_{\mathrm{obs}}$ and $_{\mathrm{mod}}$ denote the observed and modelled compositions respectively. Below a specified value of X_{sps} (in this case $X_{\mathrm{sps}} = 0.01$), a modified χ, with X_{prp} in place of X_{sps}, was used to prevent the X_{sps} term becoming excessively influential as a result of small values in the denominator.

Starting with the whole rock composition, the *P–T* point whose modelled composition best matches the measured core composition (P_1,T_1) is found by varying the end point of linear THERIAK *P–T* path calculations originating at P_0,T_0. χ is minimized as a function of *P–T* using the MATLAB function fminsearch, which implements the Nelder–Mead simplex algorithm (Nelder & Mead, 1965). χ varies smoothly with *P–T*, and a single, well-defined minimum existed in all the cases studied. The composition and volume of any garnet grown between the grt-in line and P_1,T_1 is calculated by THERIAK and progressively removed from the bulk composition; in this study, fractionation calculations were performed every 0.5 °C or 15 bar along each *P–T* path segment. Once P_1,T_1 is found, a search then begins for the next *P–T* point (P_2, T_2), whose model composition best matches the second point on the garnet transect. This procedure is repeated for every point on the garnet transect (n) and a *P–T* path constructed from multiple (n + 1) straight-line segments (Fig. 6c), along each of which there is progressive chemical fractionation. The straight-line segments join the best-fit *P–T* points, which each correspond with a point on the garnet transect. It should be noted while the volume of garnet grown is calculated, no consideration is given to its distribution in the rock – the nucleation history/density is not specified and radius-composition relationships are not considered in the modelling. In presenting the results (Fig. 6a), model compositions are plotted in the same radial position as the point on the garnet transect with which they have been matched. Matching of radial results from forward models with the observed garnet profile is carried out in a later section using THERIA_G. The time required for the script to calculate a full *P–T* path is typically a number of hours, but depends on a number of factors including the number of garnet compositions entered and the *P–T* spacing between steps.

Best-fit *P–T* path for garnet in sample DM-06-128

Application of this technique to the largest garnet in sample DM-06-128 yields an excellent match between observed and modelled garnet compositions (Fig. 6a). The resulting *P–T* path is characterized by an initial stage that involves progressive heating and burial along a linear *P–T* trend (Fig. 6d). This is followed

Fig. 6. (a) Garnet composition profile along the radial transect used for modelling; DM-06-128. The location of the profile is shown in Fig. 4e. The measured compositions are plotted, along with a polynomial curve through the data, and the values calculated by the fractionation model along the best-fit *P–T* path. The garnet composition values used to calculate the best-fit *P–T* path were taken at regular intervals from the polynomial line. In presenting the results, model compositions are plotted in the same radial position as their corresponding real data points; see text for discussion, (b) Mineral composition isopleths for DM-06-128, constructed using the bulk composition of the rock. Garnet core isopleths intersect relatively close to the garnet-in boundary. There is no rim isopleth intersection point as only the X_{prp} and X_{grs} isopleths plot in the *P–T* region of interest. X_{an} and staurolite Mg# isopleths are also shown. (c) Graphical representation of the steps carried out automatically by the MATLAB script that was written to calculate a best-fit *P–T* path. See text for full details. (d) Best-fit *P–T* path calculated by MATLAB script that matched the compositions predicted by THERIAK fractional equilibrium forward models with data from the largest garnet crystal in DM-06-128. The garnet-in curve and instantaneous garnet end-member isopleths are also plotted for selected points along the *P–T* path. (e) Modelled *P–T–t* path for sample DM-06-128. The garnet-in boundary is shown for three stages along the loop – (1) prior to garnet growth, (2) at the *P–T* point represented by the end of the modelled transect and (3) at the inferred end of garnet growth. The times marked on the diagram are those used in THERIA_G modelling, as discussed in the text. (f) Mineral composition isopleths for DM-06-128, constructed using modified bulk compositions. Garnet rim isopleths intersect tightly using a composition derived from fractionation to the end of the modelled transect. X_{an} and staurolite Mg# isopleths were plotted using the final composition established at the inferred end of garnet growth. The garnet-in boundary is also shown for the three stages along the *P–T* loop listed in (e).

by a heating-dominated stage, accompanied first by exhumation, then renewed burial. The three segments of the *P–T* path correspond with the three chemical zones (A, B, C) previously described. As evenly spaced garnet compositional data were used, the spacing of the *P–T* points indicates more rapid radial

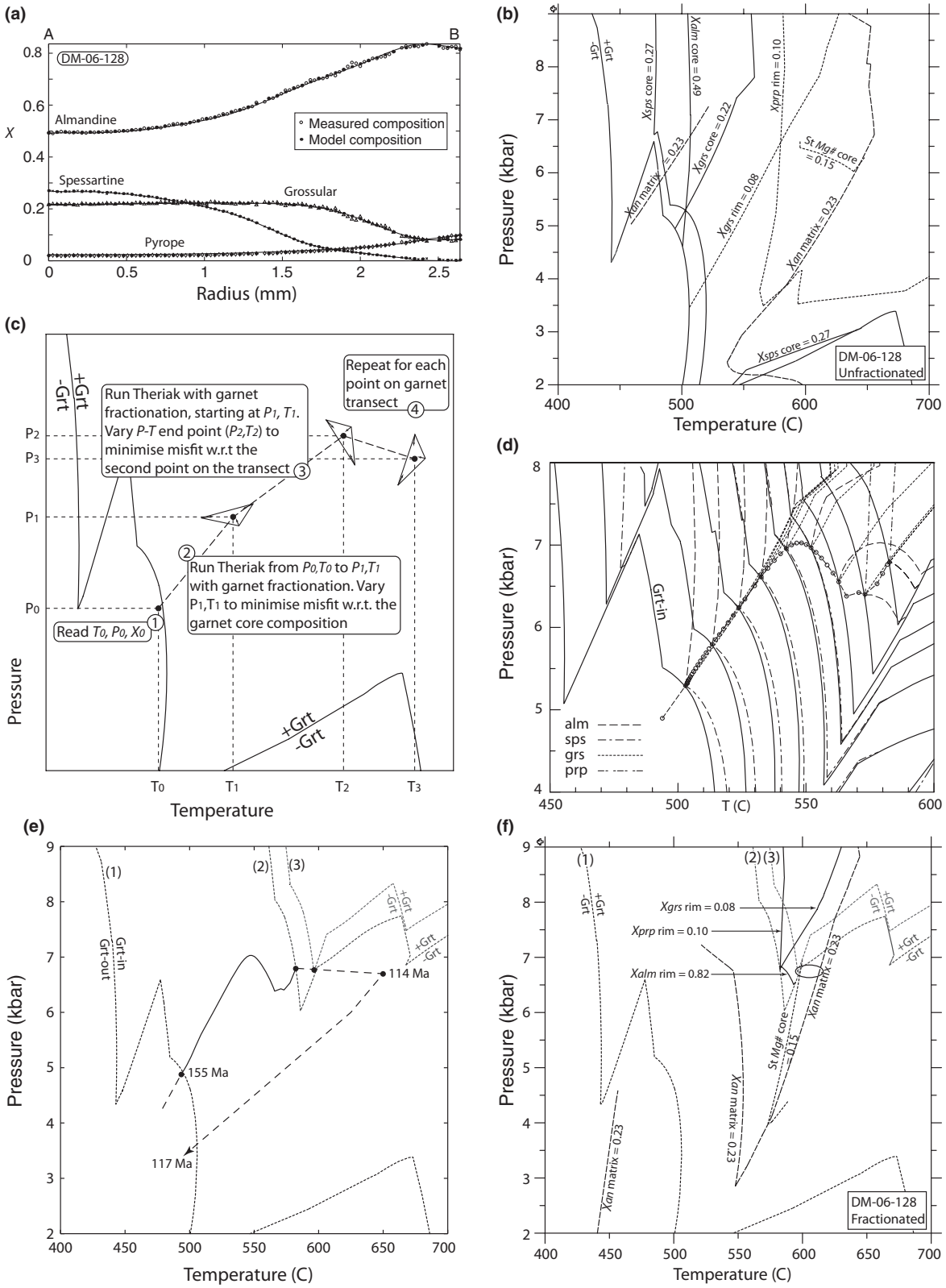

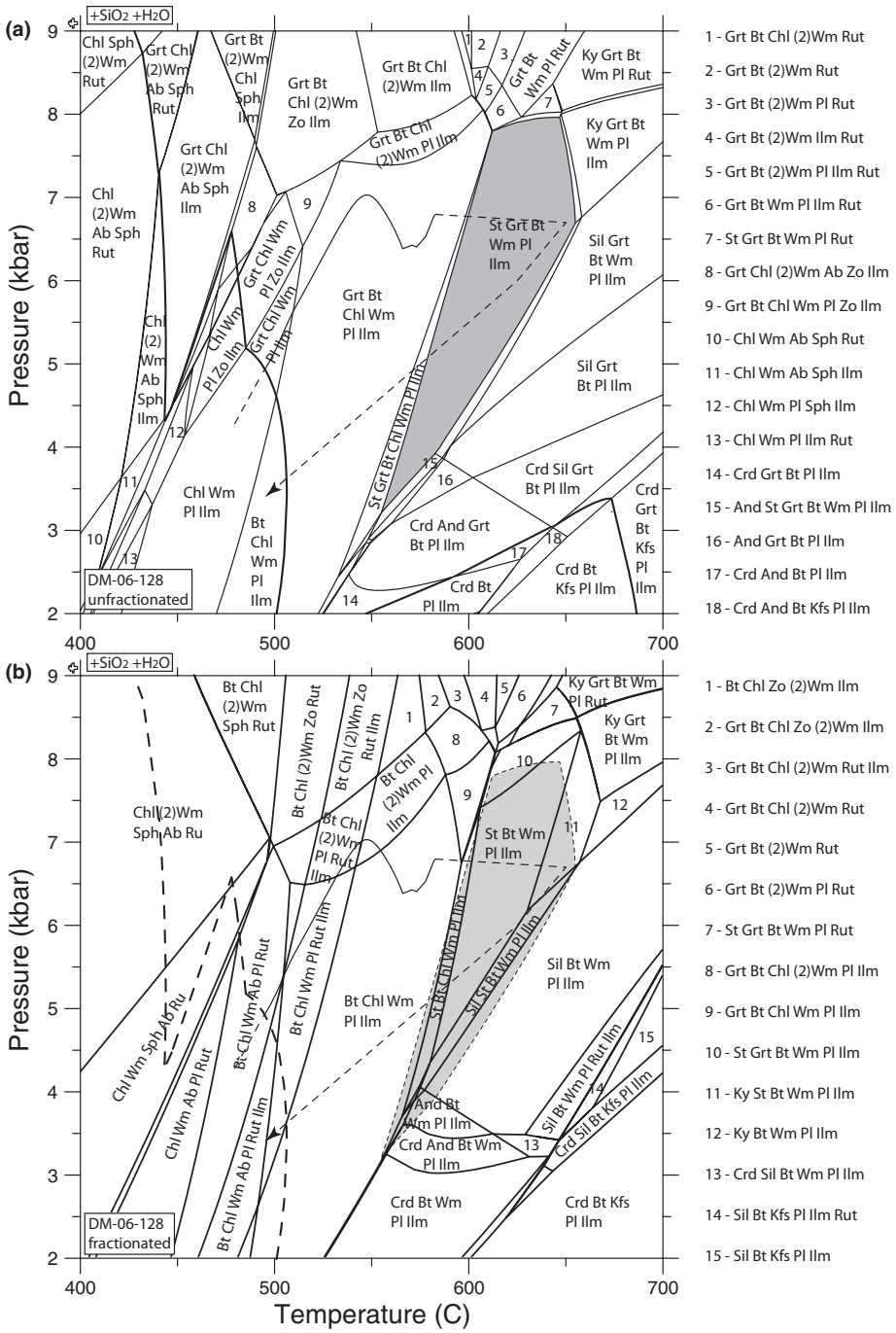

Fig. 7. (a) MnNCKFMASHT equilibrium assemblage diagram for DM-06-128. SiO_2 and H_2O are present throughout the diagram; a melt phase was not considered. Mineral abbreviations from Kretz (1983), except Wm for white mica. The field representing the peak mineral assemblages is shaded grey; (b) MnNCKFMASHT equilibrium assemblage diagram for DM-06-128, constructed using the modified composition calculated by assuming fractional equilibrium growth of garnet. The garnet-in curve from (a) is superimposed on this diagram; although fractional crystallization modelling removes garnet from the reacting rock volume, all rocks up-grade of this curve are predicted to contain garnet as part of their assemblage. In this case, the change in effective bulk composition has a limited effect on the position of other major phase boundaries. The most notable difference is the displacement of the Al_2SiO_5-in boundary towards lower temperatures at many pressures. For comparison, the position of the peak mineral assemblage field from (a) is shaded grey.

growth relative to changes in *P–T* early in the growth history of the garnet crystal, owing to the cubic relationship between the radius and volume of a spherical crystal (Gaidies *et al.*, 2008a).

The rim composition corresponds with conditions of 583 °C, 6.8 kbar; however, as there has been some resorption of the garnet, this does not represent the temperature and pressure at the end of garnet growth. In addition, the presence of kyanite in metapelite from the area (Reesor, 1973) suggests that the peak temperature reached by the rock was significantly higher than that recorded by the rim of the zoned garnet, as outlined below.

Constraints on the latter part of the prograde *P–T* path

An upper bound on the temperature reached by DM-06-128 is suggested by the absence of aluminosilicate (kyanite or sillimanite) from the mineral assemblage. The EAD for this rock predicts growth of kyanite above ~650 °C (Fig. 7a) at a minimum pressure of ~6.7 kbar. EADs constructed for other St + Grt-bearing samples in the suite and for other typical metapelites (e.g. Pattison & Tinkham, 2009) yield very similar results. These conditions also approximate the low-pressure limit required to form the Ky-St-Grt-Bt assemblage reported by Reesor (1973). An upper pressure limit of ~8 kbar is suggested by the ubiquity of ilmenite (Fig. 7a). The presence of kyanite in rocks nearby suggests that temperature could not have been significantly lower than ~650 °C, whereas temperatures higher than this would be expected to lead to widespread development of kyanite at the expense of staurolite. Combining information from different samples to produce an approximate peak *P–T* estimate of 650 °C, 6.7 kbar rests on the assumption that these samples experienced the same *P–T* conditions. This assumption is justified by their occurrence in a small area that forms part of a structurally continuous and well-defined stratigraphic sequence (Fig. 1d; Fyles, 1967).

This estimate does not take into consideration any displacement in the position of phase boundaries as a result of garnet fractionation. Although garnet fractionation may have a limited effect on the *P–T* stability range of other major phases (Evans, 2004; Zuluaga *et al.*, 2005), an increase in the bulk Mg# due to garnet fractionation coincides with displacement of the kyanite-in line to lower temperatures at many pressures. An EAD for DM-06-128 constructed using a fractionated composition (Fig. 7b) predicts that, in the extreme case, kyanite growth could start at a temperature up to 25 °C lower than is predicted for the unfractionated bulk composition. While acknowledging that 650 °C may represent a slight overestimate of the peak temperature, this figure is used in modelling the complete *P–T* path as it maximizes the potential for intracrystalline diffusion, which is considered in a later section.

Modelling of the full prograde path assuming equilibrium fractional crystallization with no intracrystalline diffusion suggests cessation of garnet growth at ~596 °C, 6.78 kbar, well below the temperature at which kyanite would be expected to grow. As the final portion of the prograde path (that which succeeds the directly modelled segment, Fig. 6d) only accounts for a small part of the total chemical fractionation, results are not very sensitive to uncertainty in peak *P–T* conditions.

Modal and compositional changes along the *P–T* path

Predicted changes in the bulk composition and mineral modes were modelled along the *P–T* loop (Fig. 8). The only change in mineral assemblage predicted during garnet growth is the introduction of biotite at ~510 °C (Fig. 8a). The end of garnet growth coincides with the introduction of staurolite.

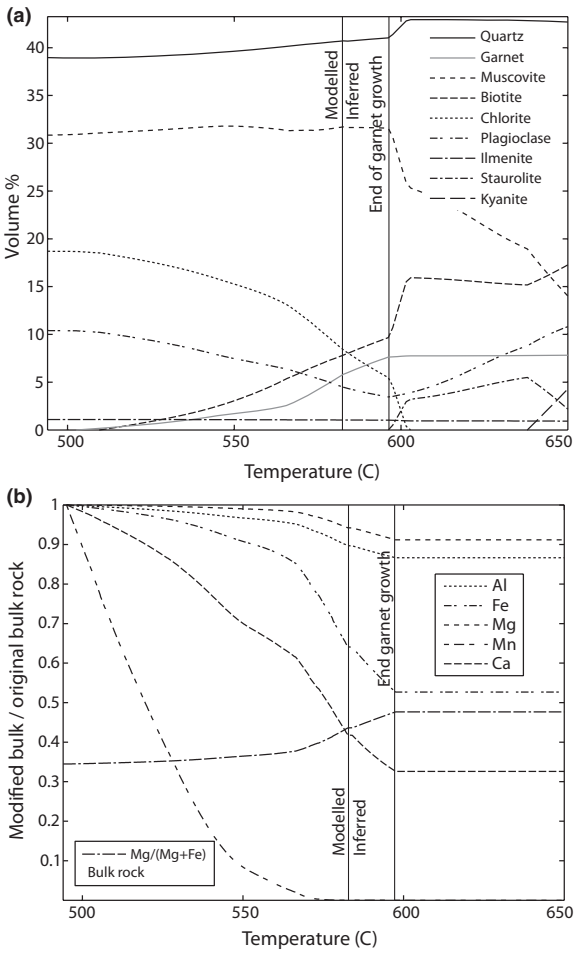

Fig. 8. (a) Predicted changes in modal mineralogy for DM-06-128 along the prograde part of the *P–T* path (Fig. 6e), assuming fractional crystallization of garnet; (b) predicted changes in the EBC of DM-06-128 along the prograde portion of the *P–T* path. Data are presented as fractions of the original composition, except in the case of $Mg/(Mg + Fe^{2+})$.

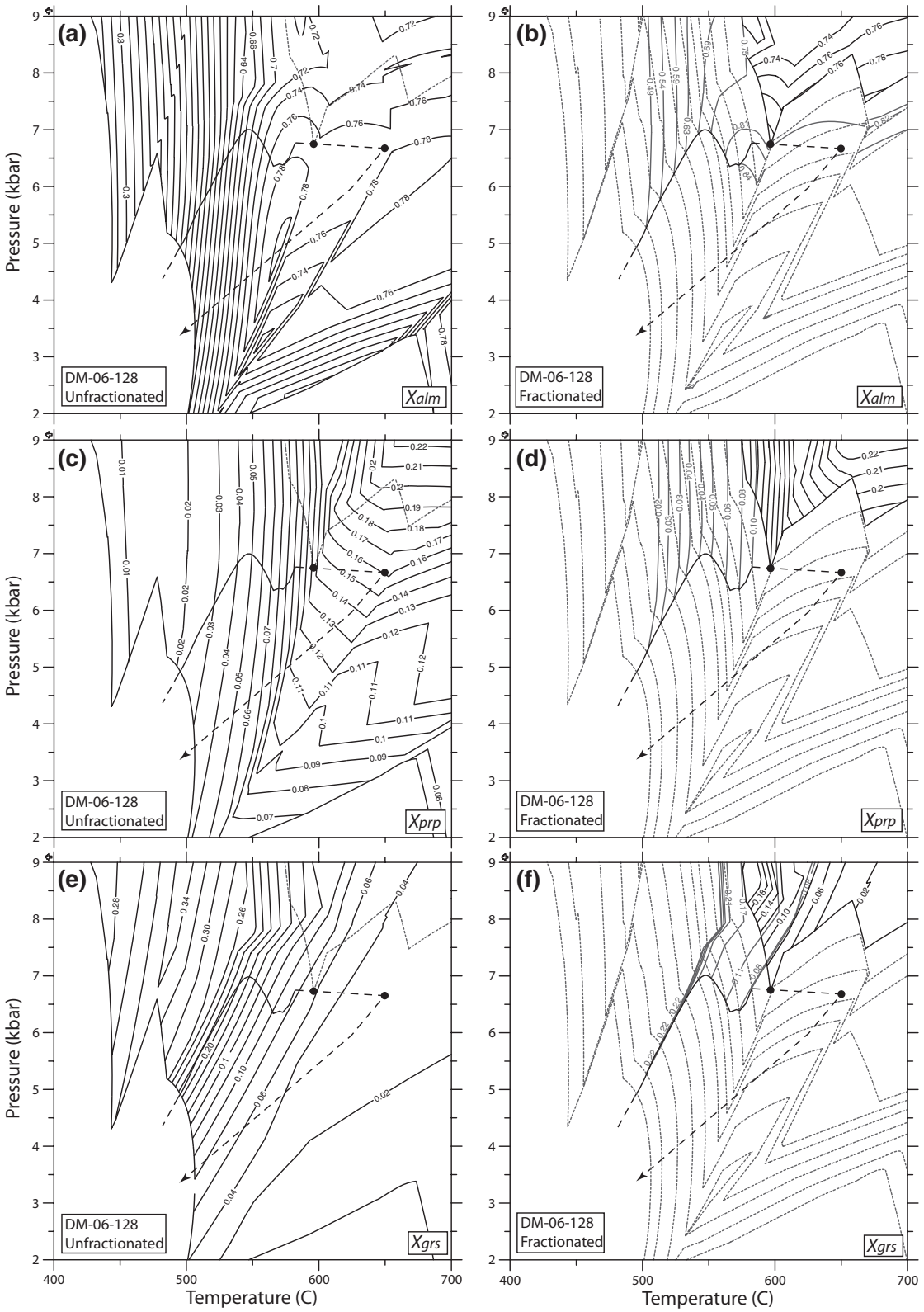

Fig. 9. Equilibrium composition diagrams for the alm, prp, grs and sps end-members of garnet. (a), (c), (e) and (g) were constructed using the bulk composition of DM-06-128. The modelled *P–T* path and the garnet-in curve at the inferred end of garnet growth are also plotted for reference. (b), (d), (f) and (h) were constructed using the fractionated composition following garnet growth. Instantaneous Grt-in curves and labelled isopleths are also plotted at ~10 °C intervals. These are shown in grey.

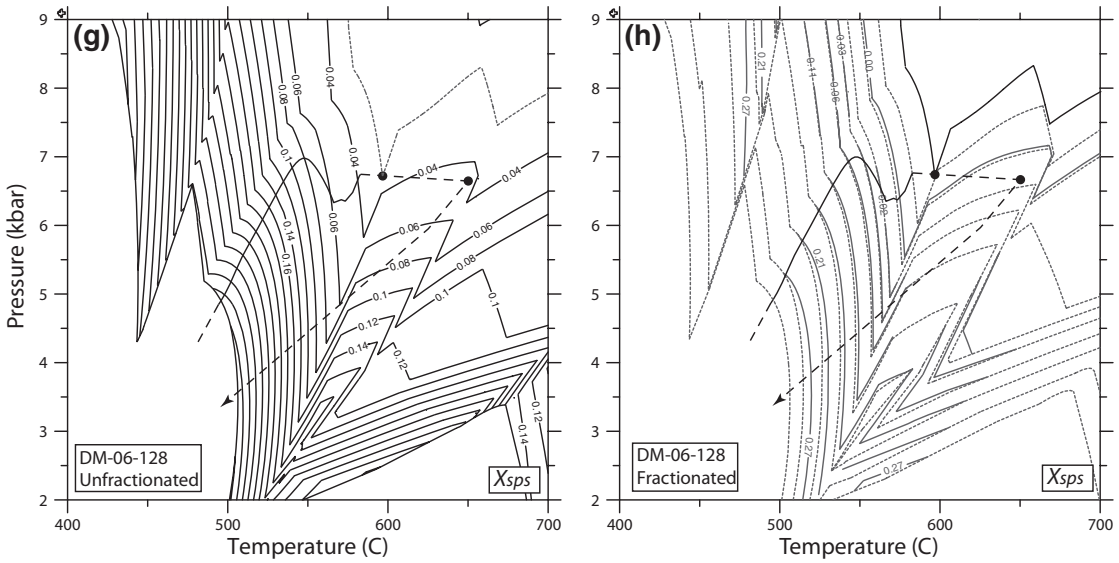

Fig. 9. (Continued)

Staurolite growth is accompanied by a marked increase in the amount of biotite at the expense of chlorite and muscovite, leading to a major pulse of dehydration before chlorite leaves the assemblage at ~602 °C, 6.77 kbar. The plagioclase mode decreases during garnet growth, but increases thereafter.

Fractionation results in a decrease in the abundance of all garnet-forming elements, but this is particularly notable in the case of Mn, which is depleted to zero, and Ca, which is reduced to close to a third of its original value. The Mg# [Mg/(Mg + Fe)] of the bulk rock composition rises from 0.35 at the onset of garnet growth to 0.43 at the end of the modelled segment, to 0.477 at the end of garnet growth (Fig. 8b).

Effect of fractionation on phase relations and mineral composition isopleths

Comparison of Fig. 7a with an EAD constructed using the fractionated composition at the end of garnet growth (Fig. 7b) shows that the change in the EBC due to fractionation is predicted to have a limited effect on major phase relations in this example, garnet excepted. The most significant change in the region of interest, as noted above, is a displacement of the Al_2SiO_5-in boundary to lower temperatures at many, though not all, pressures. This also has the effect of lowering the minimum pressure required for kyanite growth by ~0.5 kbar.

Fractionation is predicted to have a limited effect on the orientation and trend of the garnet end-member isopleths in this case (Fig. 9), but the compositional differences arising from fractionation are large enough to frustrate application of isopleth thermobarometry to rim compositions using an unfractionated bulk composition (cf. Evans, 2004; Gaidies *et al.*, 2006). The early removal of garnet from the assemblage due to fractionation has a considerable effect on the composition of some other major phases (Fig. 10). The difference between plagioclase compositions is particularly striking, with predicted X_{an} values under half those expected without fractionation (Fig. 10a,b). Significant differences are also predicted for the Mg# of staurolite and biotite (Fig. 10c–e).

The plagioclase isopleth for the measured composition (Fig. 6f) is displaced to lower temperatures, whereas the staurolite core isopleth has an orientation almost perpendicular to that calculated using the original bulk composition (Fig. 6b). The staurolite core isopleth almost perfectly intersects the point at which garnet growth is inferred to end [the downward-closing tip on the garnet-in line (3)], whereas the plagioclase isopleth is also relatively close (~15 °C higher at this pressure). There is therefore a discrepancy between the measured compositions of staurolite and plagioclase and those expected if these phases maintained equilibrium until peak conditions were reached (Figs 6f & 10a,b).

THERIA_G MODELLING OF SAMPLE DM-06-128

One of the assumptions in the modelling approach adopted above is that intracrystalline diffusion did not lead to modification of the chemical composition of garnet. Preservation of steep chemical gradients in garnet (discussed further below) supports the contention that primary zoning is preserved largely intact; however, to further test this interpretation, and investigate the likely effects of intracrystalline diffusion in the samples studied, the garnet profile from the larg-

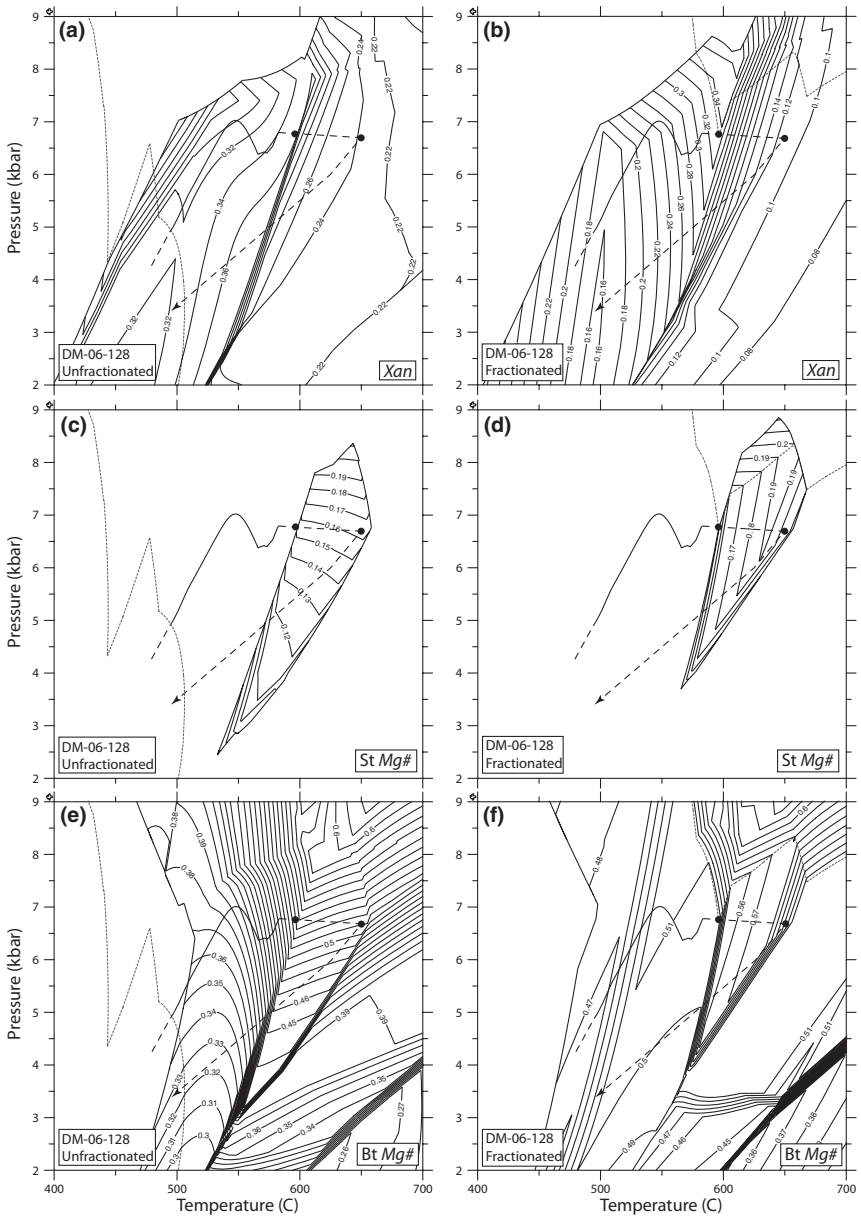

Fig. 10. Pairs of equilibrium composition diagrams for X_{an} in plagioclase and Mg# in staurolite and biotite. (a), (c) and (e) were constructed using the bulk composition of DM-06-128, whereas the fractionated composition at the end of garnet growth was used in (b), (d), (f). For reference, the garnet-in lines at the beginning and end of garnet growth are shown, as is the modelled *P–T* path.

est crystal in DM-06-128 was also modelled using THERIA_G (Gaidies *et al.*, 2008a). This program simulates the growth of a population of garnet crystals undergoing equilibrium fractional crystallization and simultaneous intracrystalline diffusion.

Input data

The three main inputs required for THERIA_G modelling are as follows: (i) a crystal size distribution (CSD), (ii) *P–T–t* data and (iii) garnet diffusion coefficients. The CSD, which records the relative abundance of garnet crystals from a given size range, accounts for the presence of crystals of varying size resulting from ongoing nucleation throughout the period of garnet growth (Gaidies *et al.*, 2008a). In this study, a CSD with nine relative size ranges (radius classes) was used. As DM-06-128 proved too coarse-grained for acquisition of a meaningful CSD using X-ray tomography, a CSD was generated by trial and error (Gaidies *et al.*, 2008b,c), based on a starting estimate with a log-normal distribution

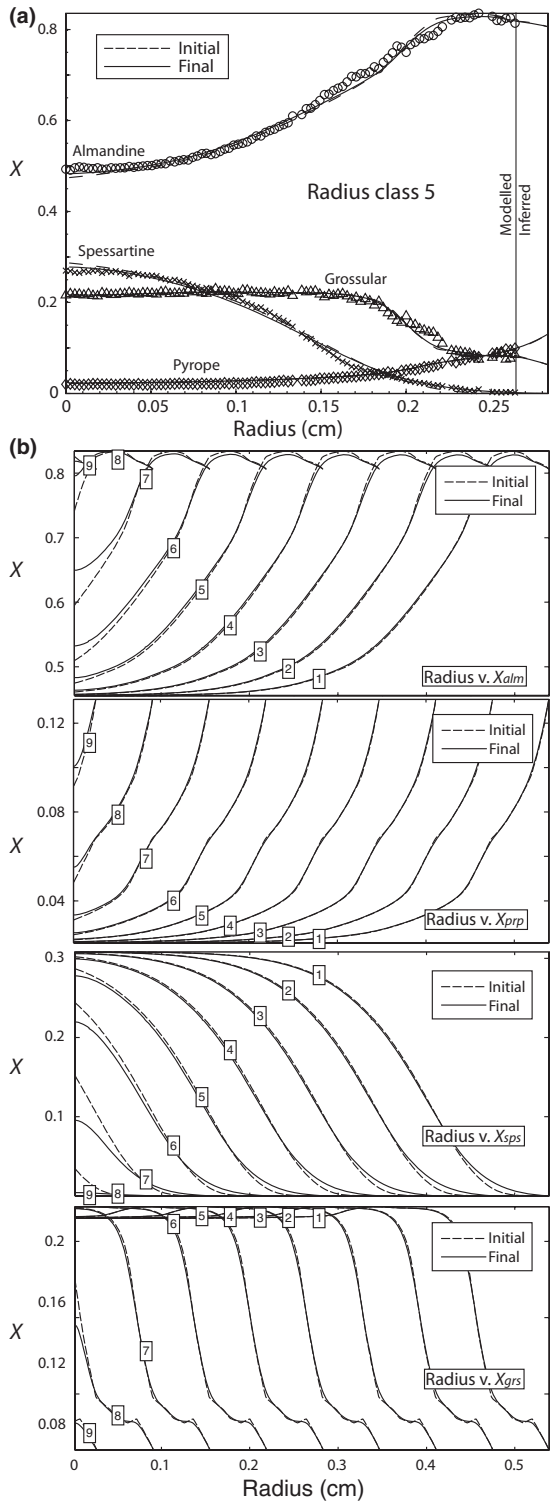

Fig. 11. (a) Results of THERIA_G modelling for radius class 5. The model results fit the data well, and there is little difference between the initial (composition at growth) and final (composition at the end of the *P–T* path) profiles; (b) results of THERIA_G modelling for all radius classes. The most significant differences between the initial and final profiles are evident in the youngest garnet crystals, particularly in the case of Fe and Mn.

(Gaidies *et al*., 2011), assuming nucleation continued throughout the modelled garnet growth history.

The *P–T* path used is that derived from the combined THERIAK-MATLAB modelling described above. Although the approximate age of peak metamorphism is known, the full thermal history is not. The approach adopted was to model a simple scenario, with a slow heating rate that would provide high potential for diffusional modification, while conforming to available geological constraints. The modelled *P–T–t* path represents an end-member rather than being a preferred geological interpretation.

The rocks under consideration underwent Barrovian metamorphism and associated D2 deformation following emplacement of the Nelson batholith, which was intruded over the interval 170–155 Ma (Leclair *et al*., 1983; Ghosh, 1995). The 117 Ma Baldy pluton was deformed during D2, indicating deformation and metamorphism persisted until this time, whereas the 114 Ma Midge Creek stock is largely post-tectonic (Leclair *et al*., 1993). In the contact aureole of the Midge Creek stock, andalusite is superimposed on regional metamorphic kyanite, demonstrating a return to upper crustal levels by the time of its emplacement (Leclair, 1988; Leclair *et al*. 1993).

The modelled *P–T–t* loop has a 41 Ma duration, which is the maximum allowed by geological constraints. The prograde portion of the path lasts 38 Ma, with a constant heating rate of 4.1 °C Ma^{-1}. A further 3 Ma is allocated to the retrograde portion of the path, with a constant cooling rate of 50 °C Ma^{-1}. All of the input parameters used in THERIA_G modelling are included in Table S1.

Results

There is a close fit between the observed radial chemical profile and that modelled for radius class 5 (Fig. 10a). For this radius class the effect of diffusion is minimal, with little modification of garnet compositions following growth. Intracrystalline diffusion results in small changes in X_{alm} and X_{sps} in the core, and some smoothing of the X_{alm} profile near the rim; however, significant differences are only apparent in the younger garnet radius classes with smaller radii (Fig. 10b). Following garnet growth, changes in the matrix composition due to 'internal metasomatism' (Spear, 1988b) are predicted to be negligible.

DISCUSSION

Textural sector zoning in garnet

The observed textural sectoral zoning and associated features resemble those described by Andersen (1984) and Rice & Mitchell (1991, and references therein). Andersen (1984) identified two categories of inclusions that are typical of TSZ garnet: type 1 inclusions are included remnants of the matrix that are concen-

trated along sector boundaries (the plane that joins the centre of the crystal with the intersection line between crystal faces). Type 2 inclusions are tubular quartz rods that extend in the growth direction – perpendicular to growth faces – and are believed to form during garnet crystallization (Andersen, 1984; Burton, 1986; Jamtveit & Andersen, 1992). Andersen (1984) and Jamtveit & Andersen (1992) attributed type 2 intergrowths to rapid non-planar crystal growth arising from supersaturation, whereas Burton (1986) favoured development of the intergrowth behind a planar crystal face at conditions close to equilibrium. Whereas the texturally zoned samples examined in this study contain abundant type 1 inclusions, type 2 intergrowths have not been observed. The streaks of slightly varying Ca concentration parallel to inclusion-free columns (Fig. 3a; Pattison & Tinkham, 2009) have the same orientation as would be expected for type 2 intergrowths, but the nature of the relationship between these phenomena is not clear.

Other distinctive textures evident in the garnet are graphite accumulations at the tips of inclusion-free columns and within rims, and in one sample (DM-06-157G) arcuate zones that resemble cleavage domes. Harvey *et al.* (1977) and Ferguson *et al.* (1980) interpreted cleavage domes to form in response to matrix displacement during porphyroblast growth. Ferguson *et al.* (1980) concluded that cleavage domes are only likely to be preserved under conditions of non-deviatoric (lithostatic) stress, because deviatoric stress would lead to augen-style wrapping of cleavage around porphyroblasts. The presence of features resembling cleavage domes in DM-06-157G may therefore indicate that the central parts of the garnet, where these textures are preserved, grew in the absence of deviatoric stress prior to penetrative D2 deformation at this location.

Ferguson *et al.* (1980) suggested that although diagnostic microstructures (i.e. cleavage domes) are only likely to be preserved in exceptional circumstances, displacement growth may be very common. Rice & Mitchell (1991) noted a near ubiquitous association between cleavage domes and TSZ, and interpreted a common origin involving displacement of insoluble matrix. The absence of parts of the zoning history from sites on the lee side of some graphite accumulations (e.g. Fig 3a) provides support for a displacement growth model. It appears that in these locations, graphite accumulated to the point where garnet growth was temporarily inhibited, leading to a localized discontinuity. These embayments were subsequently filled and planar growth faces re-established. The region outside inclusion-free columns is typically rich in fine-grained inclusions, and this textural change is interpreted to mark the end of displacement growth. As columns have different lengths (Fig. 3b), and the textural boundaries are discordant with chemical zoning, the change from displacement growth to incorporation of inclusions was diachronous and influenced by local factors.

Wilbur & Ague (2006) presented chemical maps of garnet crystals that display TSZ with type 1 inclusions and type 2 quartz intergrowths. The chemical zones in these samples have non-concentric, branching outlines that mimic the shape of inclusion-poor columns. On the basis of the results of Monte Carlo garnet growth models, these authors attributed the formation of these branched forms to supersaturation resulting from reaction overstepping. The model results predicted a transition from planar, to branched, and finally to dendritic crystal forms with increasing levels of supersaturation. Although the Kootenay Arc samples have morphological similarities with those shown by Wilbur & Ague (2006), type 2 inclusions are absent, and the chemical zoning pattern is concentric rather than branching. The concentric growth zoning indicates that the supersaturated conditions required to produce such branched forms did not exist during formation of these garnet crystals.

Formation of garnet chemical zoning

Garnet crystals display predominantly concentric zoning that is largely continuous from core to rim, suggesting a single interval of garnet growth. Although some crystals have complex internal textures, chemical zones pass through sector boundaries and similar chemical zoning is present in rocks irrespective of whether they display TSZ.

The zoning that is present in these crystals is interpreted as growth zoning that has experienced minimal modification due to diffusion. This is suggested by the preservation of steep chemical gradients, both radial and lateral, particularly at sharp 'corners' around graphite accumulations where garnet growth was impeded (Fig. 3a,c). While this is most evident in the case of Ca, these features are also visible in maps of Mn, the fastest diffusing element. Significant diffusional modification is also incompatible with discrete changes in the slopes of zoning profiles within zone B (Fig. 5). The results of THERIA_G modelling also suggest little diffusional modification would be expected in large crystals given available constraints on the thermal history.

Continuity in the compositional zoning, combined with the fact that rocks with and without staurolite share a common zoning pattern, suggests that garnet growth was by a full-system equivalent of the KFMASH reaction:

$$\mathrm{Chl} + \mathrm{Ms} + \mathrm{Qtz} = \mathrm{Grt} + \mathrm{Bt} + \mathrm{H_2O} \qquad (1)$$

prior to the development of staurolite. Staurolite would typically be expected to grow at the expense of garnet according to a full-system equivalent of the KFMASH reaction:

$$\mathrm{Grt} + \mathrm{Chl} + \mathrm{Ms} + \mathrm{Qtz} = \mathrm{St} + \mathrm{Bt} + \mathrm{H_2O}. \quad (2)$$

In this case, however, there is no evidence that garnet participated in the staurolite-producing reaction. There is no truncation of compositional zoning, nor is there an increase in Mn on the rims of garnet crystals (Kohn & Spear, 2000). Although small local discontinuities are present in some radial transects, these reflect local hiatuses in garnet growth rather than rock-wide processes. There was some replacement of the garnet rims by chlorite, but this was a low-*T*, retrograde process, as evidenced by the lack of an increase in Mn on garnet rims. The lack of evidence for prograde garnet resorption provides justification for use of a model that assumes non-reactivity of garnet, as has been documented in some natural samples elsewhere (e.g. Pattison & Tinkham, 2009).

The zoning characteristics of garnet crystals from this study resemble some of those described by Menard & Spear (1993), who noted a coincidence between a steep drop in X_{grs} and the loss of epidote from the garnet inclusion assemblage. In the samples studied here, however, the steep drop in X_{grs} does not coincide with such a change in assemblage. Three of the samples (DM-06-128, DM-06-157G, DM-06-129B) contain epidote; however, it is present in all garnet zones and in the rock matrix. The same zoning characteristics are also exhibited in garnet from DM-06-127A, in which epidote has not been detected. Epidote stability was not considered in this study as modelling was carried out in the system MnNCKFMASHT. Zoisite and clinozoisite act as proxies for epidote in this system, but are not predicted to be stable along the calculated *P–T* path (Fig. 7). Consideration of a Fe^{3+} component would, however, stabilize epidote to higher-*T*/lower-*P* conditions than is predicted for zoisite/clinozoisite in MnNCKFMASHT.

Potential non-equilibrium effects

Garnet isopleths for the core composition intersect at a point ~10 °C above the garnet-in curve. It is possible this reflects inadequacies in the thermodynamic data, solution models or bulk composition used in the modelling. A probable contributing factor, however, arises from the likelihood that the largest garnet crystal in the rock volume was not sampled and sectioned though its centre.

An alternative interpretation is that some or all of this discrepancy results from overstepped (non-equilibrium) growth of garnet. To the extent that this was the case, that is, that garnet did not grow over this interval, the calculations would represent an overestimate of the true amount of chemical fractionation. It is noteworthy, however, that the composition of garnet varies along its entire radius. There are no regions, in the core or elsewhere, of radially constant composition, as may be expected in the case of overstepped garnet growth (Zeh & Holness, 2003; Gaidies *et al.*, 2011). The radial streaks in X_{grs} discussed above are clearly a non-equilibrium phenomenon; however, their magnitude is small and they are second-order features that are superimposed on broader trends.

The *P–T* path

The compositional zoning in garnet implies three stages in the *P–T* history during garnet growth. The first segment is linear, with a dP/dT of ~0.04 kbar °C $^{-1}$. The *P–T* trajectory calculated for this segment is strongly dependent on the slope of grossular isopleths. Whereas the Holland & Powell (1998) data set was used for this study, use of an alternative database (Spear, Pattison & Cheney, discussed in Pattison *et al.*, 2002) results in a steeper dP/dT of ~0.061 kbar °C $^{-1}$ (F.S. Spear, pers. comm.).

Assuming a rock density of 2800 kg m^{-3}, the value of 0.04 kbar °C $^{-1}$ equates to burial of 7.8 km, with a temperature increase of 7 °C for every kilometre of burial. At the end of this segment, conditions of 7.03 kbar, 548 °C indicate an average instantaneous geothermal gradient of 21 °C km^{-1} for the same rock density. This is lower than typical values for continental crust and lower than current values in the southern Canadian Cordillera of ~30–35 °C km^{-1} (Hyndman & Lewis, 1995). This main phase of burial is attributed to crustal thickening during D2 deformation, which, as evidenced by microstructures, at least partly coincided with garnet growth. The low apparent thermal gradient is typical for the early, burial-dominated phase of Barrovian metamorphism (England & Thompson, 1984; Thompson *et al.*, 1997; Jamieson *et al.*, 1998).

From the end of zone A, the *P–T* path is dominated by an increase in temperature. There is a smooth transition from phase 1 into phase 2, in which heating is accompanied by decompression of ~0.6 kbar. This corresponds with garnet zone B, which is characterized by a steep fall in X_{grs}. These two growth phases represent the part of the crystal that is sector zoned.

The low Ca garnet rims (zone C) are prominent in all samples and are often texturally distinct, but except locally, where garnet growth was impeded, there are no compositional discontinuities at this boundary. Textural evidence for resorption is also lacking. The *P–T* trajectory implied by the rim compositions is highly sensitive to very small changes in X_{grs}, and caution is required in interpreting its *P–T* significance, particularly given the potential for propagation or amplification of errors through the fractionation calculations (Gaidies *et al.*, 2008a). Nevertheless, whereas fractionation changes the position of grossular isopleths, it has little effect on their orientation (Fig. 9e,f). A low or zero gradient in X_{grs}

therefore implies some increase in pressure during growth, provided that growth reflects equilibrium crystallization with a constant bulk composition. There are no igneous bodies in the study area, or other indications that there might have been metasomatism. It is possible, however, that these small changes, and the variation in X_{grs} zoning between samples (i.e. the grs annulus in DM-06-157G; Fig. 4) reflects the influence of minor phases not considered, fluctuations in fluid composition not accounted for in the modelling, or disequilibrium incorporation of Ca (e.g. Chernoff & Carlson, 1997; Konrad-Schmolke *et al.*, 2005).

Metamorphic development after garnet growth

As garnet growth ended before or with the introduction of staurolite to the assemblage, the composition of the rim was established before peak temperature conditions were reached. This composition, if preserved, could not be used to estimate peak conditions using thermobarometry; rather, in a case such as this, successful application of thermobarometry would require that the garnet rim maintain local equilibrium by intergranular diffusion over the remainder of the prograde interval. At slightly higher grades, staurolite-bearing rocks would be expected to develop kyanite. A prediction of the fractionation model, however, is that, although isobaric heating would produce aluminosilicate, it would not be accompanied by further garnet growth as the garnet-in line is displaced to higher pressure. The tendency for fractionation to reduce the *P–T* interval over which garnet grows was also noted by Spear (2010).

The position of isopleths constructed using the fractionated bulk composition at the end of garnet growth is illustrated in Fig. 6f. As biotite has been chloritized, it cannot be plotted, but in the case of plagioclase (unzoned) and staurolite there is a large discrepancy between their positions and the inferred peak *P–T* conditions. Instead of recording the compositions predicted for peak conditions, these minerals record compositions expected at, or shortly after the onset of staurolite growth. This may result from inadequacies in thermodynamic data, solution models or the fractionation path, amongst others. It is possible, however, that this discrepancy reflects a pulsed, rather than continuous reaction history. The early phase of staurolite growth coincides with a major pulse of dehydration, associated with the consumption of all remaining chlorite. The chlorite-consuming reaction has a high reaction affinity and the large fluid flux is expected to have a catalytic effect, facilitating elemental transport and lowering kinetic barriers to reaction (Waters & Lovegrove, 2002; Pattison & Tinkham, 2009; Pattison *et al.*, 2011). In contrast, reaction affinity would be expected to build slowly across the large multivariant field that the *P–T* path subsequently crosses, and a much lower fluid flux per °C is predicted. It is possible therefore that kinetic impediments to reaction could account for a failure of the rock to track the equilibrium composition.

Utility of the automated method used to calculate the *P–T* path

The method used to calculate the *P–T* path is potentially applicable to many garnet-bearing rocks in which growth zoning is preserved. Its application is likely to be successful only to the extent that the chemical system, thermodynamic data and solution models chosen adequately describe behaviour of the natural system, and that the assumptions inherent in the method are satisfied by the sample under consideration. These assumptions include maintenance of thermodynamic equilibrium with rapid transport of components relative to garnet growth, complete fractional crystallization, equivalence of the matrix composition with the EBC (cf. Spear, 2010) and lack of modification by intracrystalline diffusion. The last assumption limits its applicability to rocks that have not spent considerable time at high temperatures.

Ideally, the compositional transect used in modelling should include the oldest portion of the largest garnet in the rock volume under consideration, which will generally require the use of X-ray tomography. Failure to determine this composition adds ambiguity in interpreting the significance of any gap between the garnet-in curve and the point represented by the composition of the apparent core. Even in cases where failure to measure the oldest garnet composition is the sole reason for this gap (i.e. there was no overstepping and the bulk composition/thermodynamic data used are accurate) a linear extrapolation across this *P–T* interval is required. The larger this interval, the greater will be the potential for inaccurate fractionation calculations, the effects of which will be propagated through the entire modelled *P–T* path.

The automated method presented here will always produce a 'best-fit' *P–T* path; however, this may have little significance in cases where there is poor correspondence between real and modelled data. The most robust *P–T* information is likely to be acquired by combining modelling with extensive characterization of rock and mineral properties.

ACKNOWLEDGEMENTS

Thanks to B. Hamilton for helpful discussions and assistance with MATLAB; B. Hamilton and J. Cubley also reviewed an early version of the manuscript. Thanks to F. Gaidies for assistance with THERIA_G, to R. Marr for microprobe support, and to D. Tinkham for supplying solution models. Thanks to F. Spear, J. Ague and journal editor D. Whitney for astute reviews that helped improve the article.

Funding for this study was provided by NSERC Discovery grants to Pattison (037233) and to P. Simony.

REFERENCES

Andersen, T.B., 1984. Inclusion patterns in zoned garnets from Mageroy, north Norway. *Mineralogical Magazine*, **48,** 21–26.

Archibald, D.A., Glover, J.K., Price, R.A., Farrar, E. & Carmichael, D.M., 1983. Geochronology and tectonic implications of magmatism and metamorphism, southern Kootenay Arc and neighbouring regions, southeastern British Columbia. Part I: Jurassic to mid-Cretaceous. *Canadian Journal of Earth Sciences*, **20,** 1891–1913.

Archibald, D.A., Krogh, T.E., Armstrong, R.L. & Farrar, E., 1984. Geochronology and tectonic implications of magmatism and metamorphism, southern Kootenay Arc and neighbouring regions, southeastern British Columbia. Part II: Mid-Cretaceous to Eocene. *Canadian Journal of Earth Sciences*, **21,** 567–583.

Burton, K.W., 1986. Garnet-quartz intergrowths in graphitic pelites: the role of the fluid phase. *Mineralogical Magazine*, **50,** 611–620.

de Capitani, C. & Brown, T.H., 1987. The computation of chemical equilibrium in complex systems containing non-ideal solutions. *Geochimica et Cosmochimica Acta*, **51,** 2639–2652.

de Capitani, C. & Petrakakis, K., 2010. The computation of equilibrium assemblage diagrams with Theriak/Domino software. *American Mineralogist*, **95,** 1006–1016.

Chakraborty, S. & Ganguly, J., 1992. Cation diffusion in aluminosilicate garnets: experimental determination in spessartine-almandine diffusion couples, evaluation of effective binary, diffusion coefficients, and applications. *Contributions to Mineralogy and Petrology*, **11,** 74–86.

Chernoff, C.B. & Carlson, W.D., 1997. Disequilibrium for Ca during growth of pelitic garnet. *Journal of Metamorphic Geology*, **15,** 421–438.

Connolly, J.A.D. & Cesare, B., 1993. C-O-H-S fluid compositions and oxygen fugacity in graphitic metapelites. *Journal of Metamorphic Geology*, **11,** 379–388.

Crosby, P., 1968. Tectonic, plutonic, and metamorphic history of the Central Kootenay Arc, British Columbia, Canada. *Geological Society of America, Special Paper*, **99,** 94.

England, P.C. & Thompson, A.B., 1984. Pressure–temperature–time paths of regional metamorphism I. Heat transfer during the evolution of regions of thickened continental crust. *Journal of Petrology*, **25,** 894–928.

Evans, T.P., 2004. A method for calculating effective bulk composition modification due to crystal fractionation in garnet-bearing schist: implications for isopleth thermobarometry. *Journal of Metamorphic Geology*, **22,** 547–557.

Evenchick, C.A., McMechan, M.E., McNicoll, V.L. & Carr, S.D., 2007. A synthesis of the Jurassic-Cretaceous tectonic evolution of the central and southeastern Canadian Cordillera: exploring links across the orogen. *Geological Society of America Special Paper*, **433,** 117–145.

Ferguson, C.C., Harvey, P.K. & Lloyd, G.E., 1980. On the mechanical interaction between a growing porphyroblast and its surrounding matrix. *Contributions to Mineralogy and Petrology*, **75,** 339–352.

Florence, F.P. & Spear, F.S., 1991. Effects of diffusional modification of garnet growth zoning on *P–T* path calculations. *Contributions to Mineralogy and Petrology*, **107,** 487–500.

Fyles, J.T., 1964. Geology of the Duncan Lake area, Lardeau District, British Columbia.. *British Columbia Ministry of Mines, Energy and Resources, Bulletin*, **49,** 87.

Fyles, J.T., 1967. Geology of the Ainsworth-Kaslo area, British Columbia.. *British Columbia Department of Mines, Energy and Resources, Bulletin*, **53,** 125.

Fyles, J.T. & Eastwood, G.E., 1962. Geology of the Ferguson area, Lardeau district, British Columbia. *British Columbia Ministry of Mines, Energy and Resources, Bulletin*, **45,** 92.

Fyles, J.T. & Hewlett, C.G., 1959. Stratigraphy and structure of the Salmo lead-zinc area. *British Columbia Department of Mines, Energy and Resources, Bulletin*, **41,** 162.

Gaidies, F., Abart, R., de Capitani, C., Schuster, R., Connolly, J.A.D. & Reusser, E., 2006. Characterization of polymetamorphism in the Austroalpine basement east of the Tauern Window using garnet isopleth thermobarometry. *Journal of Metamorphic Geology*, **24,** 451–475.

Gaidies, F., de Capitani, C. & Abart, R., 2008a. THERIA_G: a software program to numerically model prograde garnet growth. *Contributions to Mineralogy and Petrology*, **155,** 657–671.

Gaidies, F., de Capitani, C., Abart, R. & Schuster, R., 2008b. Prograde garnet growth along complex P–T–t paths: results from numerical experiments on polyphase garnet from the Wolz Complex (Austroalpine Basement). *Contributions to Mineralogy and Petrology*, **155,** 673–688.

Gaidies, F., Krenn, E., de Capitani, C. & Abart, R., 2008c. Coupling forward modelling of garnet growth with monazite geochronology: an application to the Rappold Complex (Austroalpine crystalline basement). *Journal of Metamorphic Geology*, **26,** 775–793.

Gaidies, F., Pattison, D.R.M. & de Capitani, C., 2011. Towards a quantitative model of metamorphic nucleation and growth. *Contributions to Mineralogy and Petrology*, **162,** 975–993.

Ghosh, D.K., 1995. U-Pb geochronology of Jurassic to early Tertiary granitic intrusives from the Nelson-Castlegar area, southeastern British Columbia, Canada. *Canadian Journal of Earth Sciences*, **32,** 1668–1680.

Harvey, P.K., Ferguson, C.C., Lloyd, G.E. & Shaw, K.G., 1977. Arcuate cleavage zones adjacent to garnet porphyroblasts in a hornfelsed metagreywacke. *Tectonophysics*, **19,** 473–476.

Holland, T.J.B. & Powell, R., 1998. An internally consistent thermodynamic data set for phases of petrological interest. *Journal of Metamorphic Geology*, **16,** 309–343.

Hoy, T., 1977. Stratigraphy and structure of the Kootenay Arc in the Riondel area, southeastern British Columbia. *Canadian Journal of Earth Sciences*, **14,** 2301–2315.

Hoy, T., 1980. Geology of the Riondel area, central Kootenay Arc, southeastern British Columbia. *British Columbia Ministry of Mines, Energy and Resources, Bulletin*, **73,** 89.

Hyndman, R.D. & Lewis, T.J., 1995. Review: the thermal regime along the southern Canadian Cordillera lithoprobe corridor. *Canadian Journal of Earth Sciences*, **32,** 1611–1617.

Jamieson, R.A., Beaumont, C., Fullsack, P. & Lee, B., 1998. Barrovian metamorphism: where's the heat? In: *What Drives Metamorphism and Metamorphic Reactions?* (eds Treloar, P.J. & O'Brien, P. J.), pp. 23–51. Geological Society Special Publication 138, London, UK.

Jamtveit, B. & Andersen, T.B., 1992. Morphological instabilities during rapid growth of metamorphic garnets. *Physics and Chemistry of Minerals*, **19,** 176–184.

Klepacki, D.W., 1985. *Stratigraphy and Structural Geology of the Goat Range Area, Southeastern British Columbia*. Unpublished Ph.D. thesis, Massachusetts Institute of Technology, Cambridge, MA, 268 pp.

Kohn, M.J. & Spear, F., 2000. Retrograde net transfer reaction insurance for pressure-temperature estimates. *Geology*, **28,** 1127–1130.

Konrad-Schmolke, M., Handy, M.R., Babist, J. & O'Brien, P.J., 2005. Thermodynamic modelling of diffusion-controlled garnet growth. *Contributions to Mineralogy and Petrology*, **16,** 181–195.

Kretz, R., 1983. Symbols for rock-forming minerals. *American Mineralogist*, **68,** 277–279.

Leclair, A.D., 1988. *Polyphase Structural and Metamorphic Histories of the Midge Creek Area, Southeast British Colum-*

bia: Implications for Tectonic Processes in the Central Kootenay Arc. Unpublished Ph.D. thesis, Queens University, Kingston, ON, Canada, 264 pp.
Leclair, A.D., Parrish, R.R. & Archibald, D.A., 1993. Evidence for Cretaceous deformation in the Kootenay Arc on U-Pb and $^{40}Ar/^{39}Ar$ dating, southeastern British Columbia. Current Research, Part A, Geological Survey of Canada, Paper 93-1A, p. 207-220.
Loomis, T.P., 1986. Metamorphism of metapelites: calculations of equilibrium assemblages and numerical simulations of the crystallization of garnet. *Journal of Metamorphic Geology*, **4,** 201–229.
Marmo, B.A., Clarke, G.L. & Powell, R., 2002. Fractionation of bulk rock composition due to porphyroblasts growth: effects on eclogite facies mineral equilibria, Pam Peninsula, New Caledonia. *Journal of Metamorphic Geology*, **20,** 151–165.
Menard, T. & Spear, F.S., 1993. Metamorphism of calcic pelitic schists, Strafford Dome, Vermont: compositional zoning and reaction history. *Journal of Petrology*, **34,** 977–1005.
Moynihan, D.P. 2012. *Metamorphism and Deformation of the Central Kootenay Arc, British Columbia*. Unpublished Ph.D. thesis, University of Calgary, Calgary, AB, 279 pp.
Nelder, J.A. & Mead, R., 1965. A simplex method for function minimization. *The Computer Journal*, **8,** 308–313.
Parrish, R.R., Carr, S.D. & Parkinson, D.L., 1988. Eocene extensional tectonics and geochronology of the southern Omineca belt, British Columbia and Washington. *Tectonics*, **7,** 181–212.
Pattison, D.R.M., 2006. The fate of graphite in prograde metamorphism of pelites: an example from the Ballachulish aureole, Scotland. *Lithos*, **88,** 85–99.
Pattison, D.R.M. & Tinkham, D.L., 2009. Interplay between equilibrium and kinetics in metamorphism of pelites in the Nelson aureole, British Columbia. *Journal of Metamorphic Geology*, **27,** 249–279.
Pattison, D.R.M. & Vogl, J.J., 2005. Contrasting sequences of metapelitic mineral-assemblages in the aureole of the tilted Nelson Batholith, British Columbia: implications for phase equilibria and pressure determinations in andalusite-sillimanite-type settings. *Canadian Mineralogist*, **43,** 51–88.
Pattison, D.R.M., Spear, F.S., de Buhr, C.L., Cheney, J.T. & Guidotti, C.V., 2002. Thermodynamic modelling of the reaction muscovite + cordierite -> Al_2SiO_5+biotite+quartz+H_2O: constraints from natural assemblages and implications for the metapelitic petrogenetic grid. *Journal of Metamorphic Geology*, **20,** 99–118.
Pattison, D.R.M., de Capitani, C. & Gaidies, F., 2011. Petrological consequences of variations in reaction affinity. *Journal of Metamorphic Geology*, **29,** 953–977.
Read, P.B., Woodsworth, G.J., Greenwood, H.J., Ghent, E.D. & Evenchick, C.A. 1991. Metamorphic Map of the Canadian Cordillera. Geological Survey of Canada Map 1714A, scale 1:2,000,000.
Reesor, J.E., 1973. Geology of the Lardeau Map-Area, East Half, British Columbia; Geological Survey of Canada. Memoir 369, 129.
Rice, A.H.N. & Mitchell, J.I., 1991. Porphyroblast textural sector zoning and matrix displacement. *Mineralogical Magazine*, **55,** 379–396.
Simony, P.S. & Carr, S.D., 2011. Cretaceous to Eocene evolution of the southeastern Canadian Cordillera: continuity of Rocky Mountain thrust systems with zones of "in-sequence" midcrustal flow. *Journal of Structural Geology*, **33,** 1417–1434.
Spear, F.S., 1988a. The Gibbs method and Duhem's theorem: the quantitative relationships along P, T, chemical potential, phase composition and reaction progress in igneous and metamorphic systems. *Contributions to Mineralogy and Petrology*, **99,** 249–256.
Spear, F.S., 1988b. Metamorphic fractional crystallization and internal metasomatism by diffusional homogenization of zoned garnets. *Contributions to Mineralogy and Petrology*, **99,** 507–517.
Spear, F.S., 2010. Reactive bulk composition and modeling garnet. *Geological Society of America Program with Abstracts*, **42,** 565.
Spear, F.S. & Selverstone, J., 1983. Quantitative P–T paths from zoned minerals: theory and tectonic applications. *Contributions to Mineralogy & Petrology*, **83,** 348–357.
Spear, F.S., Kohn, M.J., Florence, F.P. & Menard, T., 1991. A model for garnet and plagioclase growth in pelitic schists: implications for thermobarometry and *P–T* path determinations. *Journal of Metamorphic Geology*, **8,** 683–696.
St-Onge, M.R., 1987. Zoned poikiloblastic garnets: *P–T* paths and syn-metamorphic uplift through 30 km of structural depth, Wopmay orogen, Canada. *Journal of Petrology*, **28,** 1–21.
Thompson, A.B., Schulmann, K. & Jezek, J., 1997. Thermal evolution and exhumation in obliquely convergent orogens. *Tectonophysics*, **280,** 171–184.
Tinkham, D.K. & Ghent, E.D., 2005. Estimating *P–T* conditions of garnet growth with isochemical phase diagram sections and the problem of effective bulk-composition. *Canadian Mineralogist*, **43,** 35–50.
Warren, M.J., 1997. *Crustal Extension and Subsequent Crustal Thickening along the Cordilleran Rifted Margin of Ancestral North America, Western Purcell Mountains, Southeastern British Columbia*. Unpublished Ph.D. thesis, Queens University, Kingston, ON, Canada, 361 pp.
Waters, D.J. & Lovegrove, D.P., 2002. Assessing the extent of disequilibrium and overstepping of prograde metamorphic reactions in metapelites from the Bushveld Complex aureole, South Africa. *Journal of Metamorphic Geology*, **20,** 135–149.
White, R.W., Powell, R., Holland, T.J.B. & Worley, B.A., 2000. The effect of TiO_2 and Fe_2O_3 on metapelitic assemblages at greenschist and amphibolite facies conditions: mineral equilibria calculations in the system K_2O–FeO– MgO–Al_2O_3–SiO_2–H_2O–TiO_2–Fe_2O_3. *Journal of Metamorphic Geology*, **18,** 497–511.
White, R.W., Pomroy, N.E. & Powell, R., 2005. An *in situ* metatexite-diatexite transition in upper amphibolite facies rocks from Broken Hill, Australia. *Journal of Metamorphic Geology*, **23,** 579–602.
White, R.W., Powell, R. & Holland, T.J.B., 2007. Progress relating to calculation of partial melting equilibria for metapelites. *Journal of Metamorphic Geology*, **25,** 511–527.
Wilbur, D.E. & Ague, J.J., 2006. Chemical disequilibrium during garnet growth: Monte Carlo simulations of natural crystal morphologies. *Geology*, **34,** 689–692.
Zeh, A., 2006. Calculation of garnet fractionation in metamorphic rocks, with application to a flat-top, Y-rich garnet population from the Ruhla crystalline complex, central Germany. *Journal of Petrology*, **47,** 2335–2356.
Zeh, A. & Holness, M.B., 2003. The effect of reaction overstep on garnet microtextures in metapelitic rocks of the Ilesha Schist Belt, SW Nigeria. *Journal of Petrology*, **44,** 967–994.
Zuluaga, C.A., Stowell, H.H. & Tinkham, D.K., 2005. The effect of zoned garnet on metapelite pseudosection topology and calculated metamorphic *P–T* paths. *American Mineralogist*, **90,** 1619–1628.

SUPPORTING INFORMATION

Additional Supporting Information may be found in the online version of this article at the publisher's web site:

Appendix S1. Input data for THERIA_G modelling

Received 15 December 2011; revision accepted 21 January 2013.